



1                                   **Evaluating landslide response in seismic and rainfall regime:**

2                                   **A case study from the SE Carpathians, Romania**

3           <sup>1</sup>Vipin Kumar, <sup>1</sup>Léna Cauchie, <sup>1</sup>Anne-Sophie Mreyen, <sup>2</sup>Mihai Micu, <sup>1</sup>Hans-Balder Havenith

4                                   <sup>1</sup>Georisk and Environment, Department of Geology, University of Liege, Belgium

5                                   <sup>2</sup>Institute of Geography, Romanian Academy, Bucharest, Romania

6                                   Correspondence: Vipin Kumar (v.chauhan777@gmail.com)

7   **Abstract**

8   There have been many studies exploring the rainfall induced slope failures in the earthquake  
9   affected terrain. However, studies evaluating the potential effects of both landslide triggering  
10   factors; rainfall and earthquake have been infrequent despite the rising global landslide  
11   mortality risk. The SE Carpathians, which have been subjected to many large historical  
12   earthquakes and changing climate and thus resulting in frequent landslides, is one such region  
13   that is least explored in this context. Therefore, a massive (~9.1 Mm<sup>2</sup>) landslide, situated  
14   along the Basca Rozilei River, in the Vrancea Seismic Zone, SE Carpathians is chosen as a  
15   case study area to achieve the aforesaid objective. The present state of slope reveals the Factor  
16   of Safety in a range of 1.17-1.32 with a static condition displacement of 0.4-4 m that reaches  
17   up to 8-60 m under dynamic (earthquake) condition. The Groundwater (GW) effect further  
18   decreases the Factor of Safety and increases the displacement. Ground motion amplification  
19   enhances the possibility of slope surface deformation and displacements. The debris flow  
20   prediction, implying the excessive rainfall effect, reveals a flow having 9.0-26.0 m height and  
21   2.1-3.0 m/sec velocity along the river channel. The predicted extent of potential debris flow is  
22   found to follow the trails possibly created by previous debris flow and/or slide events.

23   **Key words:** Landslide; Earthquake; Rainfall; Slope Stability; Runout; SE Carpathians.



## 24 **1 Introduction**

25 Landslides, though a normal process of hillslope erosion, pose socio-economic risk to human  
26 life and infrastructure (Froude and Petley 2018; Pollock and Wartman 2020; Kumar et al.  
27 2021). Despite the rising global landslide mortality risk, effective evaluation of disastrous  
28 influences of landslides has been infrequent (Sassa 2015; Haque et al. 2019; Klimes et al.  
29 2019). Such evaluation approaches could be regional (susceptibility/hazard/risk/vulnerability)  
30 or local (slope stability, runout prediction, monitoring/change-detection mapping) (Fell and  
31 Hartford 1997; Westen et al. 2006; Margottini et al. 2013; Hungr 2018). However,  
32 effectiveness in such approaches cannot be justified until the main landslide triggering  
33 factors; rainfall and earthquake are evaluated together. Despite the numerous case studies of  
34 rainfall induced slope failures in the earthquake affected terrain (Lin et al. 2006; Helmstetter  
35 et al. 2010; Tang et al. 2011; Durand et al. 2018; Bontemps et al. 2020), studies predicting the  
36 potential effects of both factors have been relatively rare. Necessity of such studies becomes  
37 more critical in view of an annual average of >4000 landslide related deaths worldwide in the  
38 last decade (Froude and Petley 2018).

39 Owing to the capability to represent the progressive deformation in the slope under various  
40 loading conditions, numerical modeling based analysis can be considered as one of the few  
41 approaches for effective evaluation of slope instability and associated risk (Jing 2003; Fenton  
42 and Griffiths 2008). Though the continuum modelling based approaches have been common  
43 for local scale evaluation of hillslope response (Griffiths and Lane 1999; Jamir et al. 2017;  
44 Kumar et al. 2018; 2021), their limitations in estimating large strain, particularly during the  
45 dynamic analysis makes the discontinuum modeling better option (Havenith et al.2003;  
46 Bhasin and Kaynia 2004). Apart from the stability evaluation, prediction of potential run-out  
47 during the slope failure constitutes a principal risk evaluation approach (Hungr et al. 1984;  
48 Hutter et al. 1994; Rickenmann and Scheidl 2013). Among different types of landslides,  
49 debris flows have shown the maximum outreach, relatively more fatality, and secondary  
50 effects like river damming and subsequent outburst flood (Jakob et al. 2005; Ding et al. 2020;  
51 Kumar et al. 2021). Among different run-out prediction approaches, dynamic model based  
52 Rapid Mass Movement Simulation (RAMMS) (Christen et al. 2010), Flo-2D (O'Brien et al.  
53 1993), and MassMov2D (Beguir'ia et al. 2009) have been relatively more useful  
54 (Rickenmann and Scheidl, 2013; Kumar et al. 2021).



55 In view of these understandings, the present study aimed to infer the potential response of a  
56 landslide slope under the seismic and extreme rainfall conditions using stability evaluation  
57 and runout simulation. Such simulations/modeling outputs depend upon certain input  
58 parameters and criteria, the values of which might be affected by uncertainties due to  
59 nonlinear behavior of material. Therefore, a parametric analysis is also performed to evaluate  
60 the uncertainty. In order to achieve the aforementioned objectives, a massive (~9.1 Mm<sup>2</sup>)  
61 landslide in the Vrancea Seismic Zone, SE Carpathians is chosen as a case study area. The  
62 region has been subjected to frequent earthquakes and relatively wet climatic conditions that  
63 induce frequent landslides and related socio-economic losses (Micu et al. 2013; 2016; Micu,  
64 2019; Mreyen et al. 2021).

## 65 **2 Study area**

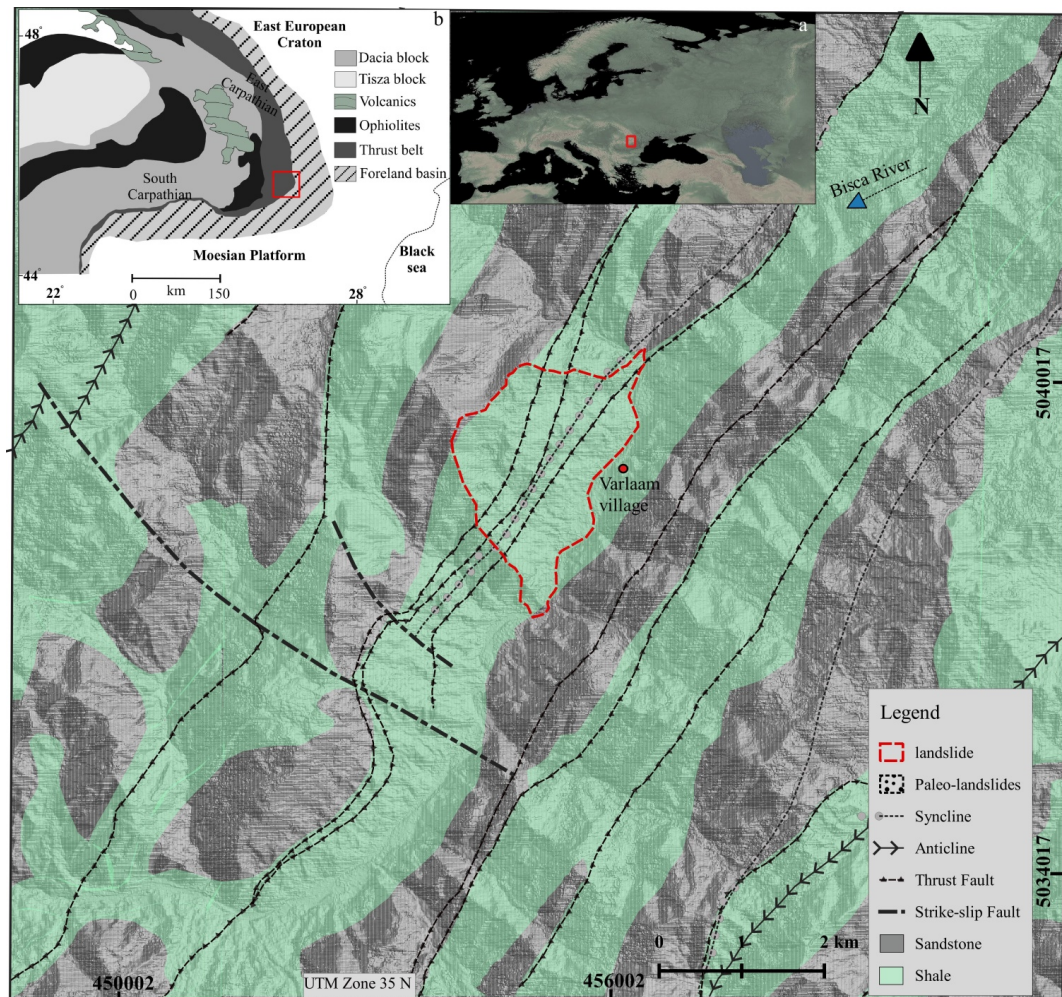
### 66 2.1 Geological setting & geomorphology

67 The landslide is situated at latitude 45° 30' 23" N, longitude 26° 25' 05" E along the Basca  
68 Rozilei River in the SE Carpathians, Romania (Fig. 1). The slope is composed of shale  
69 belonging to the Miocene thrust belt that separates the external foredeep in the north, east, and  
70 south-east from the inner Carpathians mountain ranges. Thrust faults, strike-slip faults, and  
71 folds traverse the region in and around the vicinity of landslide slope. The origin of these  
72 structural features has been related to the Eocene-Miocene collision of Alcapa and Tisza-  
73 Dacia plates against the Bohemian and Moesian promontories that gave rise to the  
74 Carpathians Mountain (Tischler et al. 2008). The SE part of the Carpathians, however, is still  
75 uplifting at a rate of 3-8 mm/yr. due to the foreland coupling of the converging plates  
76 (Pospisil and Hipmanova 2012; Maţenco 2017).

77 The landslide toe along the river hosts the 'Varlaam' village (Fig. 1, 2a). The landslide has a  
78 slope gradient ranging between 15°-20° and encompasses an area of ~9.1 Mm<sup>2</sup>. The landslide-  
79 affected area is covered by shrubs and scattered trees towards its flanks and with grasslands in  
80 the inner parts, mainly used as pastures and hayfields. The landslide crown region has a  
81 depression that might be a surficial imprint of the paleo-detachment (or depletion zone) (Fig.  
82 2b). Near the right (or southern) flank, a seasonal flow channel (or gully) emerges near the  
83 paleo-detachment depression and finally merges at the river channel (Fig. 2c). Near the left  
84 (or northern) flank, slope surface comprises flow relics, possibly of paleo-debris flow and/or  
85 slide events (Fig. 2d), as also inferred from loose/unconsolidated deposit at the slope toe (Fig.

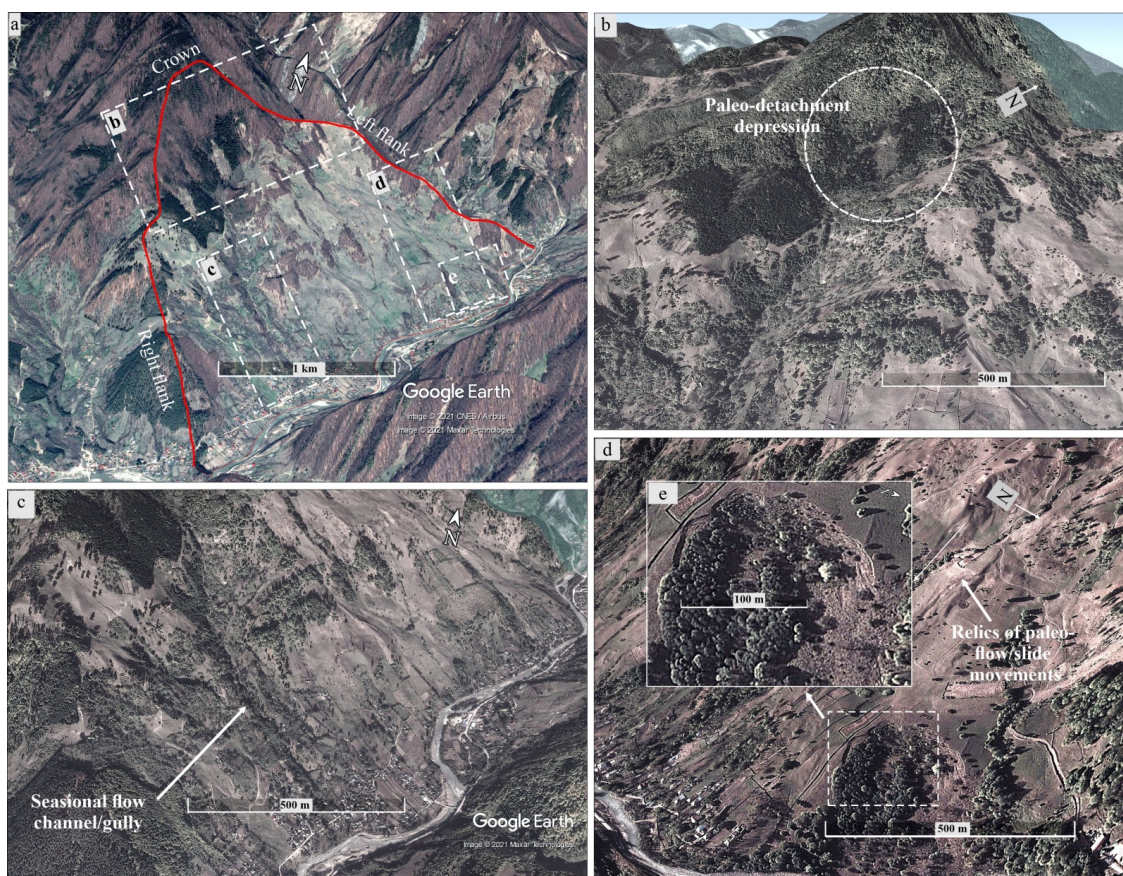


86 2e). This flow deposit is noted to develop 100-150 m wide minor scarps (Fig. 2e). Such scarps  
87 may further grow and result in the debris flows during extreme rainfall and/or earthquake  
88 events and hence pose a risk to the nearby human settlement.



89  
90 **Figure 1:** Study area. Inset 'a' (source: NOAA/NCEI, USA) 'b' (after Ustaszewski et al.  
91 2008) highlight the position of study area. Geological setting and Paleo-landslides locations  
92 are based on Murgeanu et al. 1965; Tischler et al. 2012; Pospisil and Hipmanova 2012.

93  
94  
95



96

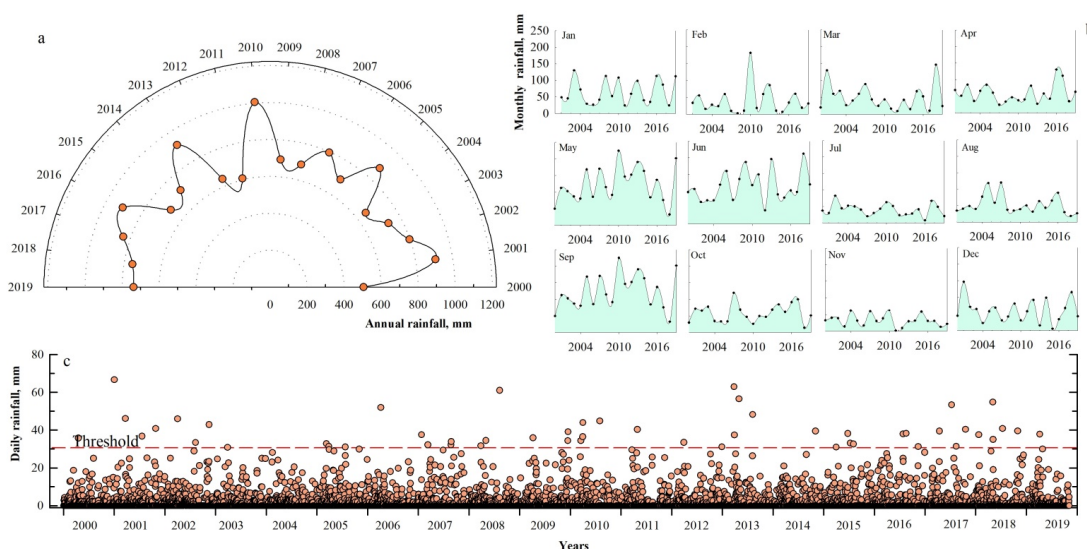
97 **Figure 2:** Landslide features. (a) Landslide marked with different features, (b) Crown portion,  
98 (c) Right flank, (d) Left flank, (e) Signs of failure in the flow deposits. Image Source: Google  
99 Earth.

## 100 2.2 Rainfall and earthquake regime

101 The average annual rainfall in the region has been  $756 \pm 120$  mm/yr during the years 2000-  
102 2019 (Fig. 3). This uncertainty of  $\pm 120$  mm/yr in average annual rainfall is referred to  
103 relatively higher annual rainfall in the last decade particularly in the years 2010, 2013, and  
104 2016 (Fig. 3a). Monthly rainfall patterns further reveal relatively higher rainfall in the months  
105 of May, June, and September in the last decade (Fig. 3b). Notably, June-September constitute  
106 the summer season in the study area. Such enhanced summer rainfall has been related to the  
107 existing positive phase of the North Atlantic Oscillation (NAO) index that allows the  
108 strengthening of continental climate, Mediterranean retrogressive cyclones, and Siberian High  
109 in central and southern Europe (Constantin et al. 2007; Magyari et al. 2013; Obrecht et al.



110 2016). Further, the daily rainfall data of the years 2000-2019 revealed 55 extreme rainfall  
111 events (Fig. 3c). ‘Extreme’ rainfall pertains to  $>30$  mm/24h in the region on the basis of  
112 previous studies exploring the rainfall variability (Apostol 2008; Croitoru et al. 2016). Out of  
113 these 55 events, 32 events with a total cumulative precipitation of about 1263 mm occurred in  
114 the last decade, particularly in the years 2010, 2013, 2016-2018.



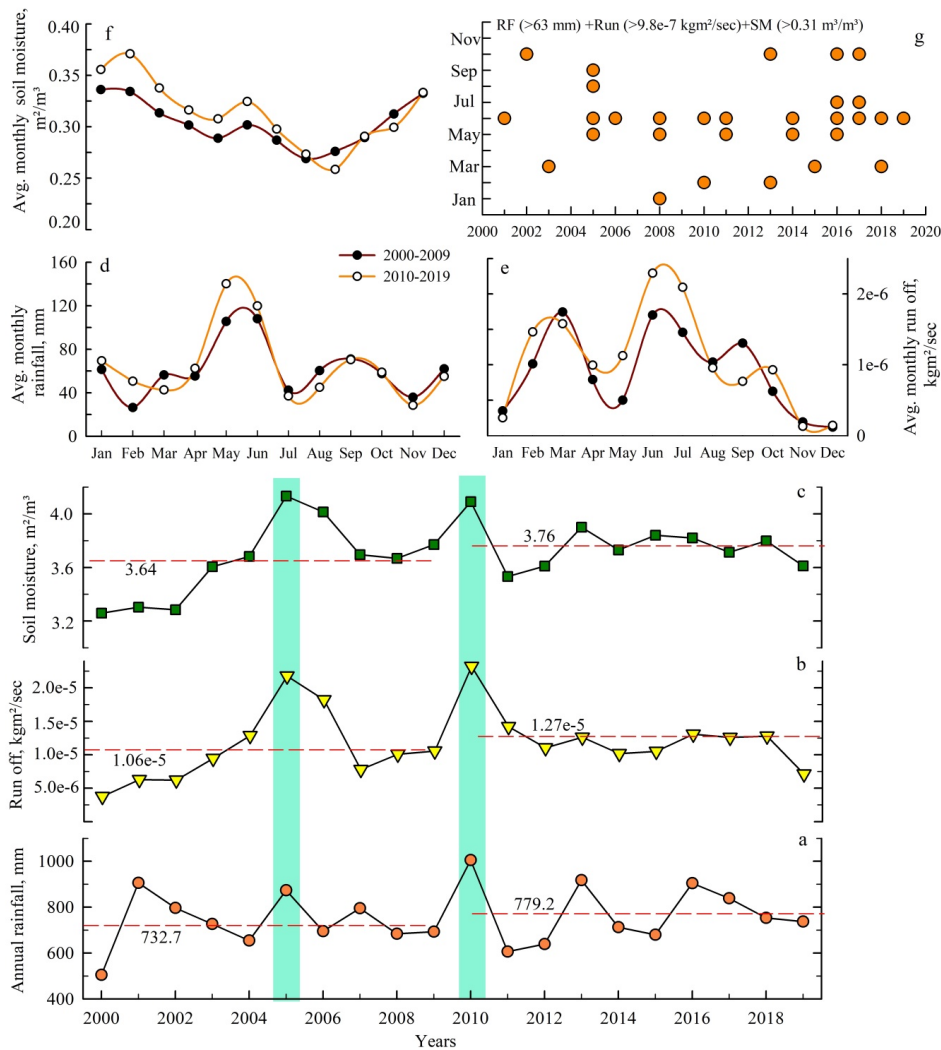
115

116 **Figure 3:** Rainfall pattern. (a) Annual variation, (b) Monthly variation, (c) Daily variation.  
117 Data source: GPM\_3IMERGDF v.06 (Huffman et al. 2019). Spatial resolution:  $0.1^\circ$ ,  
118 temporal resolution: daily. Threshold (or extreme) is based on Apostol (2008);  
119 Croitoru et al. (2016).

120 Apart from the rainfall, soil moisture and surface runoff pattern also showed temporal  
121 increase as the annual average of these parameters increased in the years 2010-2019 (Fig. 4a,  
122 b, c). The years 2005 and 2010 witnessed the peaks of all three variables that might be one of  
123 the reasons for the debris flows and flash floods in the region in these years (Micu et al. 2013;  
124 Grecu et al. 2017). The temporal increase of these parameters is also evident in the monthly  
125 regime (Fig. 4d, e, f). Further, the temporal pattern of relatively higher values (above-average)  
126 of rainfall, surface runoff, and soil moisture revealed that May-September months dominate  
127 the trend having majority of the events when all three variables had extremes (i.e., above-  
128 average) (Fig. 4g). These ‘above-average’ values refer to the monthly scale. This temporal  
129 overlapping of these variables further justifies the occurrence of debris flows and flash floods



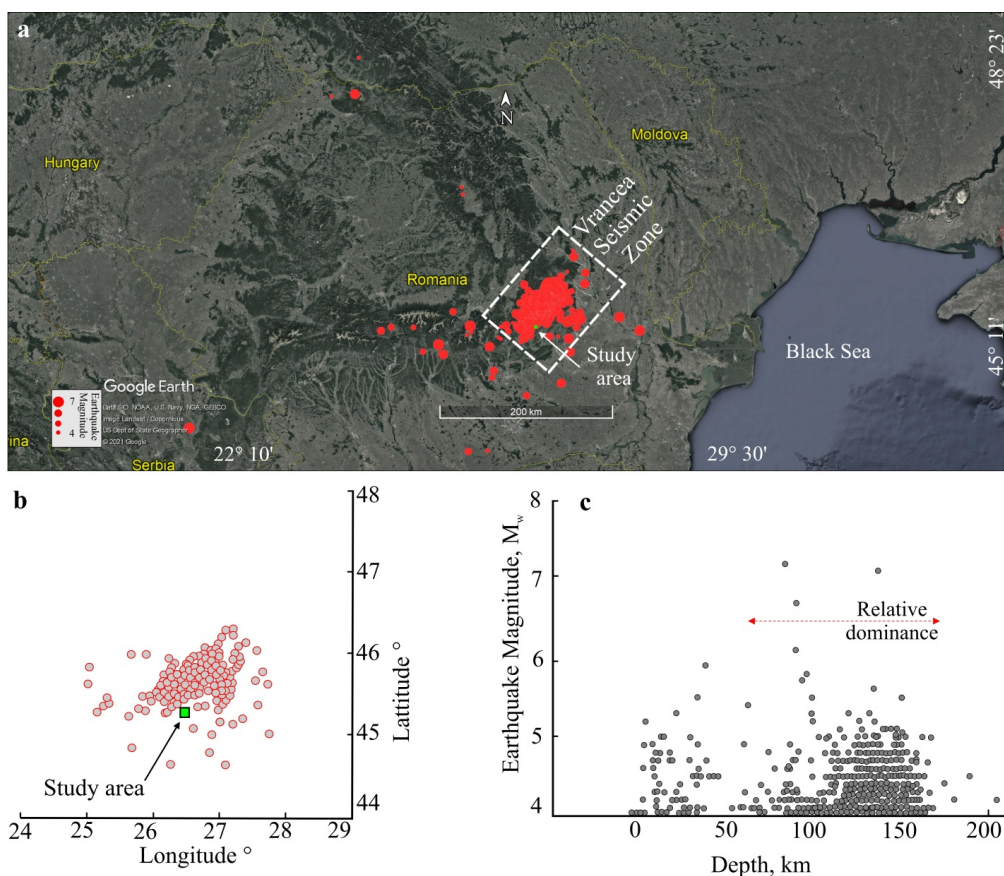
130 in this region in the last decade and possibility of more such events in the near future (Micu et  
 131 al. 2013; Ilinca 2014; Grecu et al. 2017; Micu et al. 2019).



132 **Figure 4:** Relationship of rainfall, surface runoff, and soil moisture. (a-c) Annual pattern.  
 133 Green bars refer to peaks of all three variables in these years. (d-f) Average monthly  
 134 pattern, (g) Months having above-average values of rainfall, runoff, and soil moisture.  
 135 Data Source: Surface runoff data (FLDAS\_NOAH01\_C\_GL v. 01, McNally et al.  
 136 2017). Soil moisture data (GLDAS\_CLSM025\_DA1\_D, Li et al. 2020). Spatial  
 137 resolution: 0.1°, temporal resolution: monthly.



138 Apart from the temporally enhanced rainfall, surface runoff, soil moisture, the study area is  
139 also subjected to frequent earthquakes owing to its position in the Vrancea Seismic Zone that  
140 is one of the most active seismic zones in Europe (Fig. 5).



141

142 **Figure 5:** Earthquake pattern. (a-b) Position of study area (c) Depth and Earthquake  
143 magnitude. Data source: National Institute for Earth Physics, Romania.

144

145 This region has received  $\sim 490$  earthquakes ( $M_w \geq 4$ ) during the years 1960-2019. The  
146 earthquake event cluster represents a NE-SW trend (Fig. 5b). About 75 % of the total  
147 earthquake events occurred in a depth range of 60-180 km (sub-crustal depth) and 4 out of 5  
148 events having a magnitude  $\geq 6$  occurred within 60- 100 km depth (Fig. 5c). The relative  
149 dominance of  $M \geq 6$  earthquakes in this depth range has been related to the reverse faulting  
150 mechanism in this depth range (Radulian et al. 2007; Petrescu et al. 2019). The possible



151 explanation of the pattern of earthquakes has been divided in the following two  
152 categories; (1) it might be associated with descending relic ocean lithospheric beneath the  
153 bending zone of the SE Carpathians , or (2) it might be associated to continental lithosphere  
154 that has been delaminated, after the collision (Bokelmann and Rodler, 2014; Petrescu et al.  
155 2019). These frequent earthquakes in the region have caused many landslides and any major  
156 future earthquake might have ground effects in a much larger area (150000 km<sup>2</sup>), possibly  
157 causing more landslides (Havenith et al. 2016).

### 158 **3 Methodology**

159 In order to evaluate the landslide response under seismic and extreme rainfall conditions, our  
160 approach involved data collection from field and numerical simulations (slope stability and  
161 runout analysis). Details are as follows;

#### 162 3.1 Debris (or loose material) depth estimation

163 We analysed seismic ambient noise at 56 measure points to estimate the depth of impedance  
164 contrasts. The equipment was composed of 7 velocimeters Güralp CMG-6TD 30s and 1  
165 velocimeter Lennartz 5s and Cityshark II. The technique aims at estimating the site resonance  
166 frequency by computing the spectral ratio between horizontal (NS, EW) and vertical  
167 components (Nakamura, 1989). Under particular geological conditions where impedance  
168 contrast exists at depth, as representative of a loose/soft material overlying bedrock, the  
169 resulting Horizontal to vertical spectral ratio (HVSr) curve presents a peak in correspondence  
170 of the site resonance frequency ( $f_s$ ). Fig. 6a represents the location of the inferred  $f_s$  in a range  
171 of <1.5-4.5 Hz. Lower frequencies, generally implying relatively higher thickness of loose  
172 material, are noted in the central part and near the right flank.

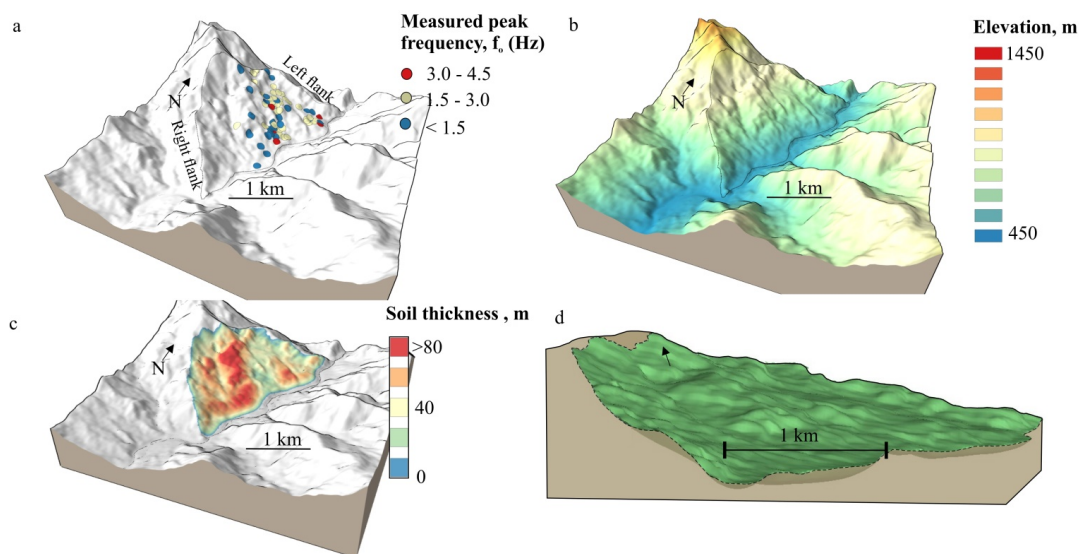
173 The thickness ( $h$ ) of the loose/soft material is consecutively estimated using the shear-wave  
174 velocity ( $V_s$ ) and resonance frequency ( $f_s$ ) using the following equation (Murphy et al. 1971;  
175 Ibs-von Seht & Wohlenberg 1999);

$$176 \quad h = V_s / (4 * f_s) \quad \text{Eq. 1}$$

177 In view of the similar litho-tectonic conditions and spatial proximity, the shear-wave velocity  
178 ( $V_s$ ) values in the present study are based on Mreyen et al. (2021). For the loose overburden  
179 (soil) and rockmass, the  $V_s$  are taken as ~400 m/sec and ~900 m/sec, respectively.



180 The thickness of the loose material (inferred from the HVSR and  $V_s$ ) at different measurement  
181 locations was later imported in the LeapfrogGeo software (v. 5.1) along with the surface  
182 morphology (Fig. 6b). The surface morphology with a spatial resolution of 12 m is based on  
183 the TanDEM-X (TerraSAR-X add-on for Digital Elevation Measurement) digital elevation  
184 model. The surface morphology and depth information of loose material were integrated using  
185 the LeapfrogGeo (v.5) to construct a continuous soil thickness layer and hence a 3D model of  
186 the landslide (Fig. 6c, d). This model was later used to extract the 2D slope sections (CS-1,  
187 CS-2, CS-3, and CS-4) for the slope stability evaluation (Fig. 7a).

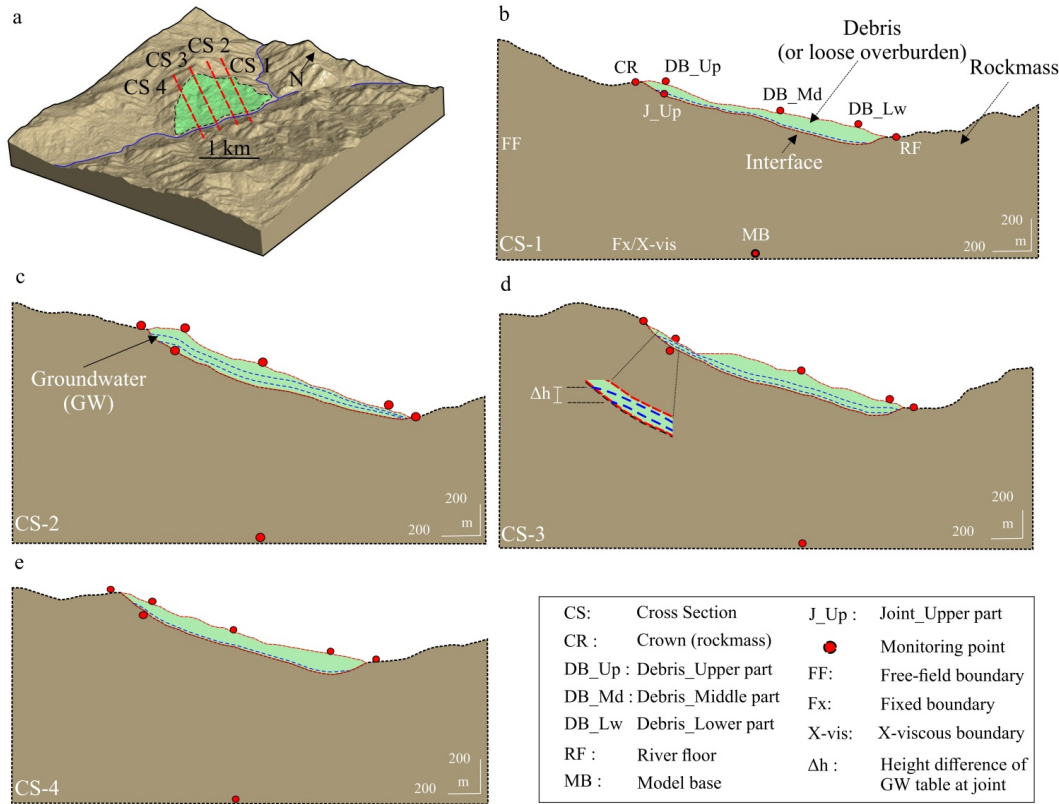


188

189 **Figure 6:** Landslide model construction. (a) Measured peak frequency distribution. Based on  
190 Cauchie et al. 2019, (b) Digital elevation model, (c) Soil (or debris) thickness pattern in the  
191 landslide, (d) Cross sectional view of landslide model.  
192

### 193 3.2 Slope Stability evaluation

194 The 2D slope sections (CS-1, CS-2, CS-3, and CS-4) were used to determine the hillslope  
195 response under static (gravity) and dynamic (seismic) conditions by performing the slope  
196 stability analysis in the UDEC v.6 (2014) software. The configuration of these 2D sections is  
197 presented in Fig. 7. Each slope section comprises loose overburden (soil) over rockmass and  
198 an interface joint separating these blocks.



199

200 **Figure 7:** Model configuration for the Slope stability analysis. (a) Landslide model. The  
 201 location of the different cross sections used in the UDEC models are marked by red lines, (b-  
 202 e) Configuration of the sections; CS-1 to CS-4.  
 203

204 Under static condition, factor of safety of slope and potential material displacement are  
 205 determined, whereas under dynamic condition, potential material displacement, Peak Ground  
 206 Acceleration (PGA), and spectral ratio are evaluated. For the PGA and spectral ratio, material  
 207 models are considered as elastic, whereas for the factor of safety and material displacement  
 208 (static/dynamic) calculations, elasto-plastic models are considered. Elastic material model  
 209 involved modulus (elastic/shear/bulk) values of the rock mass and soil. In elasto-plastic  
 210 conditions, Modified Hoek-Brown (MHB) plasticity criteria (Hoek et al. 2002) and Mohr-  
 211 Coulomb (M-C) plasticity criteria (Coulomb 1776; Mohr 1914) are used for the rock mass  
 212 and soil, respectively. The joint plane is assigned Coulomb-Slip criteria (Coulomb 1776) in



213 both elastic and plastic conditions. For dynamic analysis, two different signals, i.e. Ricker  
214 wavelet (Ricker 1943) and a signal record of the 1976 Friuli Earthquake, are used (Fig. 8).

215

216 **Figure 8:** Seismic signals. (a)  
217 Ricker Wavelet (as recorded at  
218 the model base monitoring  
219 point) (b) 1976 Friuli  
220 Earthquake, (Italy). Note:  
221 Different time scale.

222

223

224

225

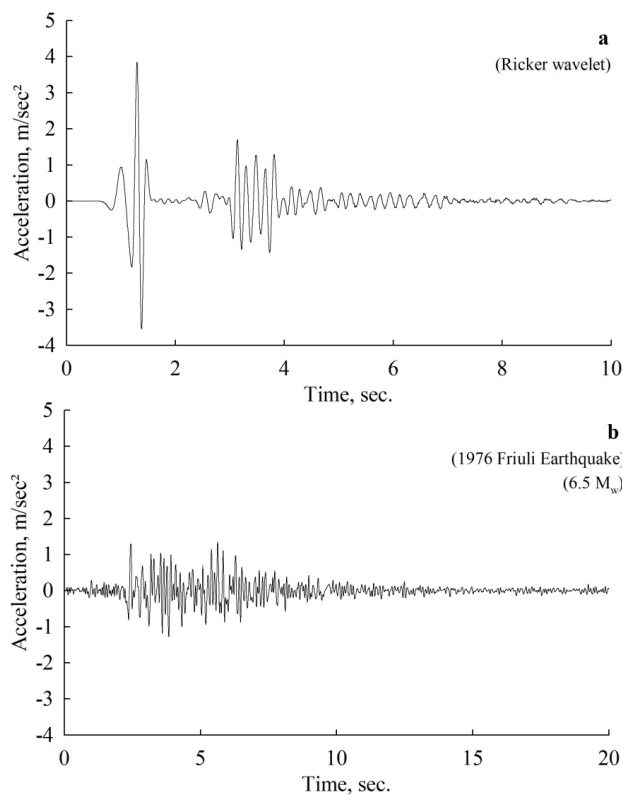
226

227

228

229

230



231 The Ricker wavelet, a theoretical waveform, provides an advantage to be a relatively short  
232 signal marked by an energy distributed over a range of frequencies. Therefore, the PGA and  
233 spectral ratio are evaluated using the Ricker wavelet to understand the ground motion  
234 amplification on the landslide surface. Notably, in many studies such ground motion  
235 amplification is found to enhance the slope instability (Lenti and Martino 2012; Gaudio et al.  
236 2014). The Ricker wavelet has been used in several studies owing to its reliable representation  
237 of seismic waves propagating through the viscoelastic homogeneous media (Bourdeau et al.  
238 2004; Gholamy and Kreinovich 2014). Further, the displacement is determined using both  
239 dynamic signals (Ricker wavelet and Friuli earthquake, 1976) to evaluate the difference.



240 Soil and rock mass blocks in the sections (CS-1 to CS-4) were discretized into finite  
 241 difference zones of 6m and 20m size, respectively according to the following relation  
 242 (Kuhlemeyer and Lysmer, 1973);

$$243 \quad \Delta l \leq \lambda/10 \text{ or } \leq \lambda/8 \quad \text{Eq. 2}$$

244 Here,  $\Delta l$  = zone size,  $\lambda$  = wavelength associated with the dominant frequency. ‘ $\lambda$ ’ can be  
 245 determined using  $\lambda = C/f$ , where  $C$  is the speed of wave propagation associated with the  
 246 fundamental frequency ( $f$ ). For the ‘ $C$ ’ (or shear wave velocity) of soil and rock mass, we  
 247 used 400 m/sec and 900 m/sec, respectively (sec. 3.1). The ‘ $f$ ’=2.0-4.5 Hz was considered as a  
 248 central frequency range. The boundary conditions were fully restrained (base) & X-restrained  
 249 (lateral) under static load and free field (lateral) & fixed/X-viscous (base) under dynamic load  
 250 (Fig. 7). To approximate the natural attenuation in the models during the seismic loading,  
 251 Rayleigh damping with a 0.02 damping ratio (i.e., 2% fraction of critical damping and 2.5 Hz  
 252 central frequency was used with the both mass and stiffness damping. Though most of the soil  
 253 types and rock mass possess the damping in the 2%-5% fraction of the critical damping  
 254 (Biggs 1964), plasticity models (M-C criteria) and presence of joints result in further energy  
 255 loss (UDEEC v.6 2014). Therefore, the damping ratio was kept at the lower level of the  
 256 suggested range.

257 Since, the area is subjected to temporally enhanced rainfall (sec. 2.2) and some studies have  
 258 noted the percolation of rainfall water in the loose material resulting in the Groundwater  
 259 (GW) level increase and subsequent slope instability (Van Asch et al. 1999; Liang 2020),  
 260 effect of the GW was also explored. The GW was included in static as well as in dynamic  
 261 analysis in plasticity conditions. The UDEEC allows the GW simulation through the joints as  
 262 per the parallel plate model (Witherspoon et al. 1980). The parameters and their values used  
 263 in the static and dynamic analysis are mentioned in Table 1.

264 Table 1: Input parameters and their values used in the static and dynamic analysis.

Rockmass parameters	values	Rockmass-soil interface (joint) parameters	values	Soil parameters	value
Density, $\gamma$ (kg/m <sup>3</sup> )	2500	<sup>4</sup> Normal Stiffness, $k_n$ (MPa/m)	10000	Density, $\gamma$ (kg/m <sup>3</sup> )	1900
<sup>1</sup> Uniaxial Compressive Strength, $\sigma_{ci}$ (MPa)	30	Shear Stiffness, $k_s$ ( $k_n/10$ )	1000	<sup>2</sup> Poisson's Ratio	0.43



<sup>2</sup> Poisson's Ratio	0.4	<sup>5</sup> Cohesion, c (MPa)	0.01	<sup>2</sup> Young's Modulus, E (MPa)	869
<sup>2</sup> Young's Modulus, E (MPa)	5670	<sup>6</sup> Friction angle, $\emptyset$	30°	<sup>2</sup> Bulk Modulus, K (MPa)	2070
<sup>2</sup> Bulk Modulus, K (MPa)	9450	<sup>7</sup> Residual aperture at high stress, m	0.0001	<sup>2</sup> Shear Modulus, G (MPa)	304
<sup>2</sup> Shear Modulus, G (MPa)	2025	<sup>7</sup> Aperture for zero normal stress, m	0.0005	<sup>5</sup> Cohesion, c (MPa)	0.01
<sup>3</sup> GSI	30	Water density, Gg/m <sup>3</sup>	0.001	<sup>5</sup> Friction angle, $\emptyset$	28°
<sup>3</sup> Material Constant (m <sub>i</sub> )	17± 4	<sup>7</sup> Joint permeability, (1/MPa*s)	10 <sup>8</sup>		
m <sub>b</sub>	1.3954	<sup>1</sup> It was inferred from the empirical equation of Kahraman (2001) using the Vs and Vp data of Mreyen et al. (2021). <sup>2</sup> These values were inferred from the empirical equations of McDowell (1990) using the P & S wave velocity of Mreyen et al., (2021). <sup>3</sup> Based on Hoek and Brown (1997) and field observation. <sup>4</sup> It was inferred from from the empirical equations of Barton (1972); Hoek and Diederichs (2006) using the elastic modulus of rock and approximated spacing of joint sets of-5-10cm. This spacing was assumed in view of highly sheared nature of rockmass. <sup>5</sup> Based on Bednarczyk (2018); Peranić et al. (2020) due to similar litho- tectonic conditions. <sup>6</sup> Based on Barton and Choubey (1977). <sup>7</sup> Based on UDEC v.6 (2014).			
s	0.004				
a	0.5223				
<sup>3</sup> D	0				

265 A parametric analysis was also performed to justify the selection of values of different input  
 266 parameters by evaluating the change in the output parameters in response to the change in  
 267 different input parameters. Out of four slope sections, the CS-2 and CS-3 were chosen to  
 268 perform the parametric analysis in view of their central position in the landslide and the  
 269 heterogeneity in soil thickness and topography (Fig. 7c, d). In order to understand the effect of  
 270 the GW level change, two GW levels were considered in the CS-2 and CS-3 sections. Since  
 271 the UDEC simulates the fluid flow through joint aperture, the GW level change is manifested  
 272 by different heights (h1, h2) of the GW at the joint. Here, the difference of h1 and h2 i.e.,  $\Delta h$   
 273 is 10m (Fig. 7d). Among the different input parameters listed in Table 1, angle of internal  
 274 friction of soil, joint friction angle, groundwater head, and elastic modulus were used for the  
 275 parametric analysis. It is to note that the bulk and shear modulus were also changed along  
 276 with elastic modulus because all three modulus parameters are interrelated (Mc Dowell 1990).  
 277 Though each parameter might have a certain effect on the output, these four have been noted  
 278 to affect the Factor of Safety and displacement relatively more (Kumar et al. 2021).

279



280 3.3 Run-out simulation

281 The hillslopes affected by the seismic shaking have also been noted to be more prone to  
 282 rainfall induced slope failures, particularly in the form of debris flows (Shieh et al. 2009;  
 283 Tang et al. 2011). Such debris flows can initiate either by increased pore pressure or runoff  
 284 involving entrainment (Godt and Coe 2007). Thus, the increased frequencies of the extreme  
 285 rainfall, soil moisture, surface runoff, and recent debris flows events in the region (sec. 2.2),  
 286 escalate the possibility of debris flow in the Varlaam landslide.

287 To ascertain the outreach of such potential debris flow during an extreme rainfall event,  
 288 Voellmy friction law based model was simulated using the Rapid Mass Movement Simulation  
 289 (RAMMS) software. The RAMMS divides the frictional resistance into a dry-Coulomb type  
 290 friction ( $\mu$ ) and viscous-turbulent friction ( $\xi$ ) (Christen et al. 2010). The frictional resistance  $S$   
 291 (Pa) is thus;

$$292 \quad S = \mu N + (\rho g u^2) / \xi \quad \text{Eq. 3}$$

293 Where  $N = \rho h g \cos(\phi)$  is the normal stress on the running surface,  $\rho$ = density,  $g$ = gravitational  
 294 acceleration,  $\phi$ = slope angle,  $h$ = flow height and  $u = (u_x, u_y)$ , consisting of the flow velocity in  
 295 the  $x$ - and  $y$ -directions.

296 Generally, the values for  $\mu$  and  $\xi$  parameters are achieved using the reconstruction of real  
 297 events through simulation and subsequent comparison between dimensional characteristics of  
 298 real and simulated event. However, the toe of Varlaam landslide merges with the river floor  
 299 and hence there is an uncertainty in reconstruction of the volume of previous flow events that  
 300 has been washed away by the river. Therefore,  $\mu$  and  $\xi$  are taken in view of topography of  
 301 landslide slope and run-out path, landslide material, and based on previous studies/models  
 302 (Hurlimann et al. 2008; Rickenmann and Scheidl 2013; RAMMS v.1.7.0). In this study,  
 303 maximum allowable friction ( $\mu$ ) i.e.,  $\mu = 0.4$  (or  $\phi = 21.8^\circ$ ) was used with the turbulence ( $\xi$ ) of  
 304  $250 \text{ m/sec}^2$  (Table 2).

305 Table 2: Details of input parameters for run-out analysis.

306 307 308	Landslide	Material type <sup>1</sup>	Material depth <sup>2</sup> , m	Friction coefficient <sup>3</sup>	Turbulence coefficient <sup>4</sup> , m/sec <sup>2</sup>
	Varlaam	Clayey Silt	5, 10, 15, 20	$\mu = 0.4$	$\xi = 250$

<sup>1</sup> Field based approximation.<sup>2</sup> Considering that fact that during slope failure, irrespective of type of trigger, entire loose material might not slide down, the depth is taken as a variable.<sup>3</sup> In order to keep the results of conservative nature & presence of vegetation, we have taken a maximum allowable friction i.e.,  $\mu = 0.4$  (Hung et al., 1984; RAMMS v.1.7.0). This case is



309 considered to understand the potential impacts of debris flow even after the maximum friction. <sup>4</sup>This range is used in view of  
310 the type of loose material i.e., cohesive (RAMMS v.1.7.0).

## 311 **4 RESULTS & DISCUSSION**

### 312 4.1 Slope stability evaluation

#### 313 4.1.1 Factor of Safety (FS) & displacement

314 The FS of slope varies in a range of 1.17-1.32 that decreases further to 1.09-1.29 under  
315 Groundwater (GW) condition (Fig. 9). In both cases, the CS-2 model attains lowest FS  
316 implying relatively more instability. The displacement in loose material was obtained in  
317 static, static with fluid (GW), dynamic, and dynamic with fluid (GW) conditions. Under the  
318 static condition, displacement ranges between 0.4-4.0 m that increases to 0.68 m-18 m under  
319 the GW condition with minimum at CS-1 and maximum at CS-2 (Fig. 9). Under dynamic  
320 condition, displacement ranges from 8-60 m, and further increases to 7.5-62 m by combining  
321 dynamic with GW conditions. Similar to the static condition, minimum displacement is noted  
322 at CS-1, whereas maximum at CS-2. Further, in all sections (CS-1 to CS-4), displacement  
323 accumulated mostly at the upper part of the debris layer (i.e., landslide crown) or at the  
324 steepest portion of slope surface. This spatial affinity of displacement and steep gradient is  
325 caused by the influence of topography on the material displacement (Kumar et al. 2021). It is  
326 to note that this dynamic displacement pattern pertains to the Friuli earthquake signal (Fig.  
327 8b). A comparison of the static and dynamic displacement (caused by the Friuli earthquake  
328 signal and Ricker wavelet) is presented in Fig. 10.

329 As also shown in Fig. 9, the GW condition enhanced the displacement in static as well as in  
330 dynamic conditions (Fig. 10). Static displacement showed least scattering as evident from the  
331 median level and least difference of Max. and Min. values. Further, except for the CS-2  
332 section, all three sections (CS-1, 3, 4) have relatively low dynamic displacement in dry and  
333 wet (GW) conditions due to the Ricker wavelet than compared to the displacement caused by  
334 the Friuli signal (Fig. 10a-d). This difference may be attributed to the response of steep  
335 topography (of CS2 model) to the multi-frequency signal (Ricker wavelet).

336

337

338

339

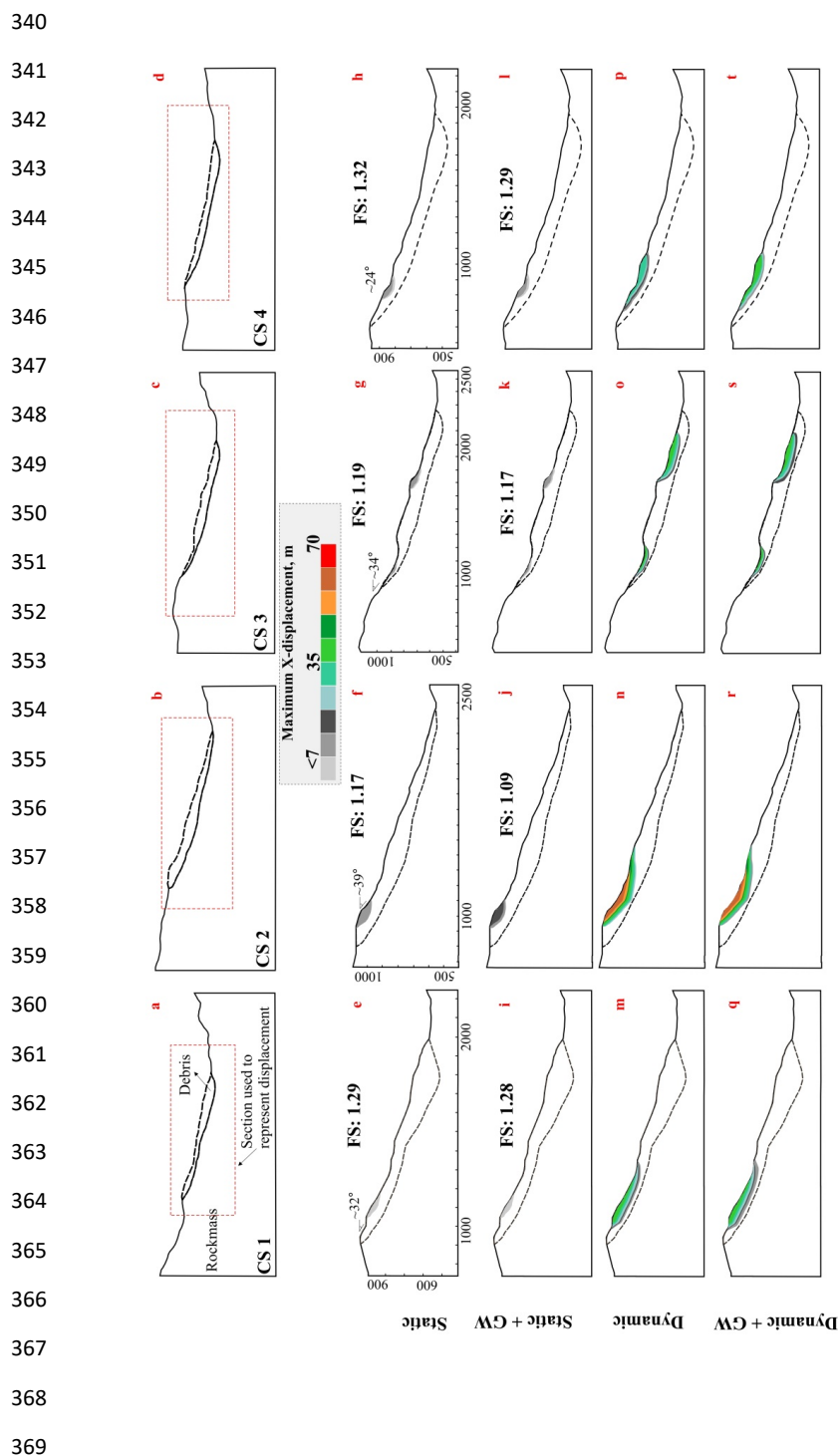
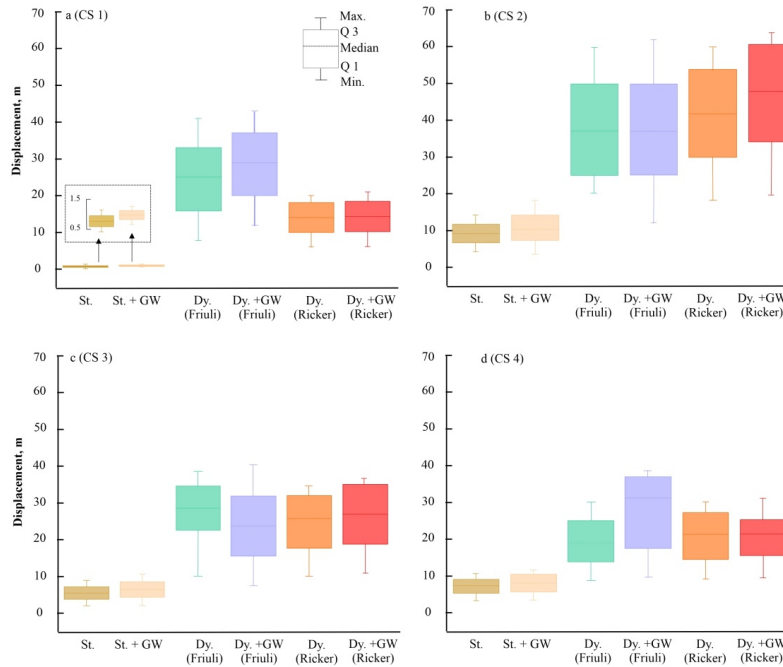


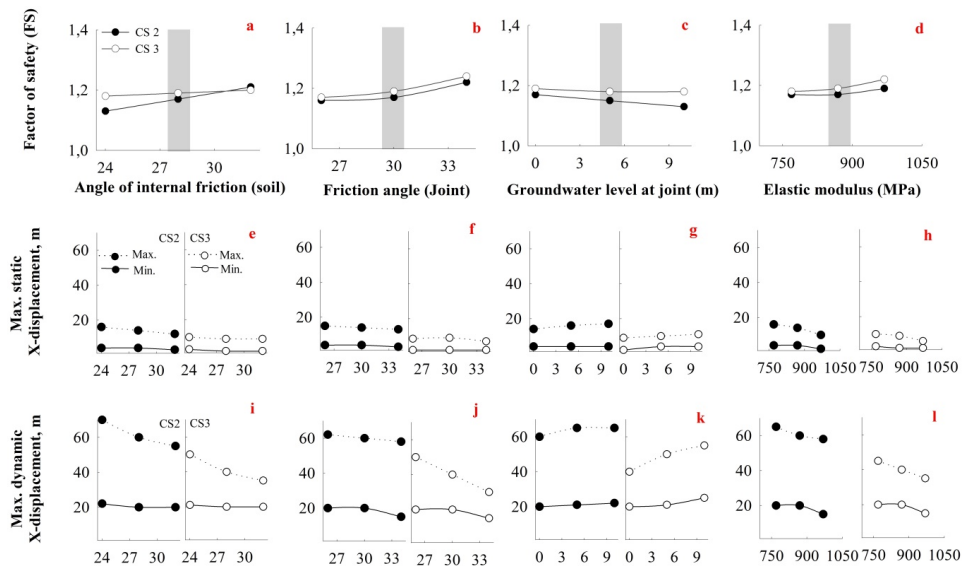
**Figure 9:** Factor of Safety (FS) and material displacement (X-direction). a – d refer to original slope sections with sub-sections (red rectangle) used to represent displacement. e – h, i–l, m–p, and q–t refer to displacement in static, static +GW, dynamic, and dynamic +GW conditions, respectively.



370  
 371  
 372  
 373  
 374  
 375  
 376  
 377  
 378  
 379  
 380  
 381  
 382



383 **Figure 10:** Comparison of material displacement under different conditions. St. and Dy. Refer  
 384 to Static and Dynamic conditions, respectively. GW refers to Groundwater.



385  
 386  
 387  
 388

386 **Figure 11:** Parametric analysis. (a-d) Variation in the FS, (e-h) Variation in the static  
 387 displacement, (i-l) Variation in the dynamic displacement. Grey bar represents the  
 388 values that are used in the slope stability analysis (sec. 4.1.1).



#### 389 4.1.2 Parametric analysis

390 The Factor of Safety (FS) of slope increased in response to increase in angle of internal  
391 friction of soil, joint friction, and elastic modulus (Fig; 11). Relatively higher increase in the  
392 FS (~7% in the CS 2) is attained by increasing the angle of internal friction of soil. This effect  
393 is attributed to the ‘Shear Strength Reduction (SSR)’ approach (Matsui and San 1992;  
394 Griffiths and Lane 1999) that was used to determine the FS. The GW level increase resulted  
395 in a decreasing FS because the increased GW level increased the joint flow rate, as per  
396 ‘Parallel-Plate model’ (Witherspoon et al. 1980), and thus enhanced the fluid pressure on the  
397 overlying medium i.e., soil. This increased fluid pressure further decreased the normal stress  
398 and hence the shear stress of the overlying soil, as per Mohr's Criteria (Mohr 1914). Such  
399 decrease in the shear stress of soil resulted in the decreased FS.

400 Since material displacement is a spatially variable parameter, as shown in Fig. 9, Static and  
401 dynamic displacements are represented in a range of maximum (max.) and minimum (min.) in  
402 Fig. 13. Static displacement is noted to decrease on increasing the angle of internal friction of  
403 soil, joint friction, and elastic modulus. Relatively higher decrease (~40% in CS 2 and ~38 %  
404 in CS3) occurred in response to the modulus increase. This decrease in the displacement is  
405 referred to fact that increased modulus increases the normal and shear strength of the soil and  
406 hence displacement will decrease on increasing the modulus (Hara et al. 1974). The GW level  
407 increase resulted in the increased static displacement (~16% in CS2, ~36% in CS3). Such  
408 increase in the static displacement is attributed to the decreased shear strength of soil due to  
409 the increased joint fluid pressure (Witherspoon et al. 1980).

410 Similar to the static displacement, dynamic displacement decreased on increasing the angle of  
411 internal friction of soil, joint friction, and elastic modulus and increased on increasing the GW  
412 level. Along with the modulus, angle of internal friction of soil is also noted to decrease  
413 (~16% in the CS2, ~21% in the CS 3) the dynamic displacement relatively more. The increase  
414 in the GW level resulted in 8% and 33% increase in the CS2 and CS3 models in dynamic  
415 displacement.

416 Notably, present study utilized approximated values of the input parameters for the slope  
417 stability analysis (Table 1). Though approximated values cannot replace the values measured  
418 in the geotechnical analysis, parametric analysis minimizes the uncertainty caused by  
419 selection of specific values by exploring the possible output pattern.



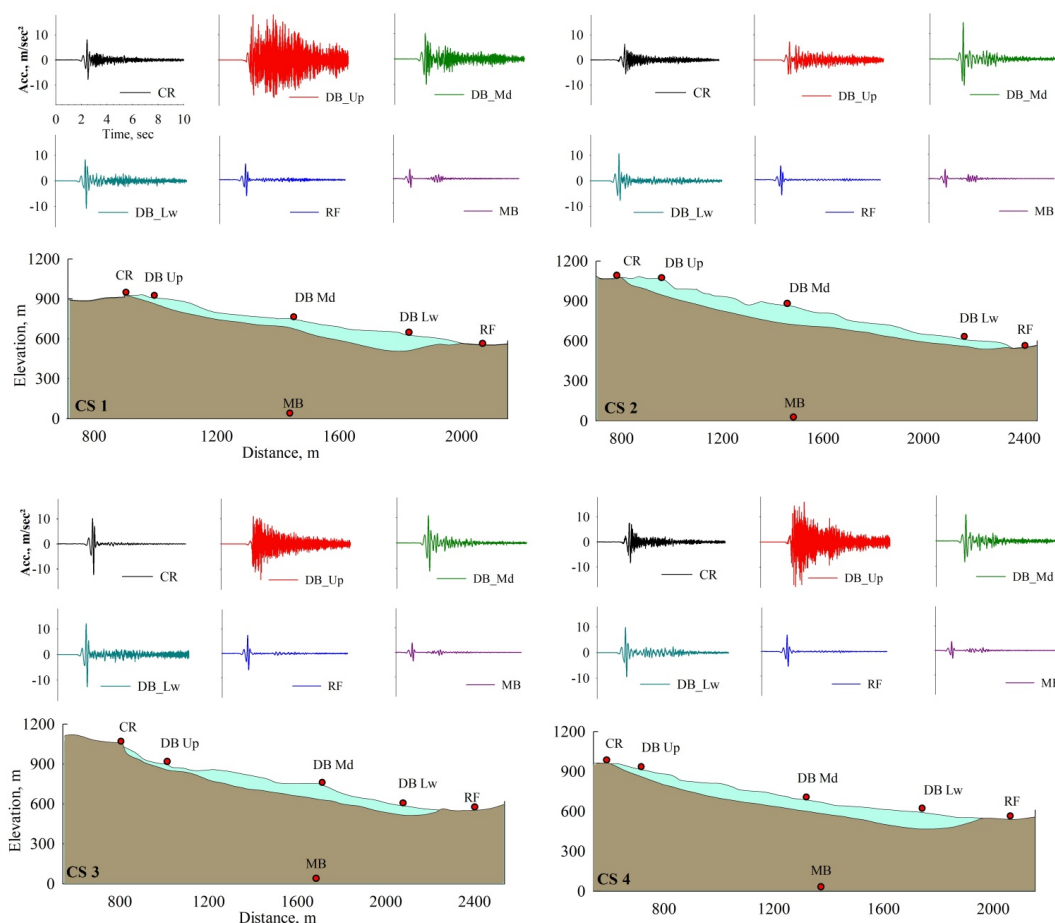
420 Thus, aforementioned findings of the parametric analysis highlight the potential uncertainty in  
421 the FS and material displacement (static/dynamic) that can arise due to the input values. By  
422 utilizing the central values (highlighted as grey) in the slope stability findings (sec. 4.1.1), the  
423 present study attempted to minimize such uncertainty in the findings. Further, though the GW  
424 was also used in the UDEC models to infer the influence of saturation on slope stability,  
425 potential response of the slope under excessive saturation (extreme rainfall) is further  
426 explored through the runout prediction (sec. 4.2).

#### 427 4.1.3 Peak Ground Acceleration (PGA)

428 Apart from the FS and displacement, ground motion (acceleration) amplification was also  
429 evaluated to understand the potential seismic deformation at the slope surface. The input  
430 seismic signal for the following acceleration pattern is presented in Fig. 8a. For all four  
431 models (CS1 to CS4), the PGA values at the river floor (RF) ranges between 5.78-7.47 m/sec<sup>2</sup>  
432 (0.58g – 0.74g), whereas at the rock mass surface above the landslide crown (CR) it varies  
433 from 6.37 to 10.19 m/sec<sup>2</sup> (0.65g -1.03g) (Fig. 12). At the model base (MB), maximum  
434 acceleration remains between 3.79-3.90 m/sec<sup>2</sup> (0.38g -0.39g).

435 Thus, the PGA at the river floor (RF) amplifies~1.5-2.0 times from the maximum acceleration  
436 at the model base, whereas at the rock mass surface above the landslide crown, it amplifies  
437 ~1.7-2.7 times from the maximum acceleration at the model base. Such amplification of the  
438 PGA at the rock mass surface above the landslide crown can be attributed to the topographic  
439 irregularity and upward propagation of seismic waves where they meet preceded waves  
440 produced on the relatively horizontal surface of the slope (Jibson 1987; Havenith et al. 2003;  
441 Bourdeau and Havenith 2008; Luo et al. 2020).

442 The debris surface, however, attains relatively higher PGA in all four models than the rock  
443 mass surface as noted at the following three monitoring stations; DB\_Lw, DB\_Md, and  
444 DB\_Up (Fig. 12). At the lower part of the debris (DB\_Lw), the PGA ranges from 8.3 to  
445 12.13 m/sec<sup>2</sup> (0.84g-1.23g) that further grew at the middle part of the debris (DB\_Md) and  
446 attains10.17-14.40 m/sec<sup>2</sup> (1.03g-1.46g). The maximum PGA is attained by the upper part of  
447 the debris (DB\_Up) with a range of 7.26-18.50 m/sec<sup>2</sup> (0.74g - 1.88g). Such relatively high  
448 PGA at the debris surface can be referred to the impedance contrast between underlying rock  
449 mass and overlying soil and/or partial loss of the shear strength during seismicity (Novak and  
450 Yan, 1990; Safak, 2001).



451  
 452 **Figure 12:** Maximum acceleration at different monitoring points. CR: Crown (Rock mass),  
 453 DB Up: Debris upper part, DB Md: Debris middle part, DB Lw: Debris lower part, RF: River  
 454 Floor, MB: Model base.

455

456 Detailed evaluation at different monitoring points in each model are as follows; Model Base  
 457 (MB) and River floor (RF) monitoring points have almost similar maximum acceleration  
 458 values in all four models. At the lower part of the debris i.e., DB\_Lw, relatively higher PGA  
 459 is attained by the CS3 model (~12.1 m/sec<sup>2</sup>) followed by the CS2 model (~10.8 m/sec<sup>2</sup>) in  
 460 comparison to DB\_Low points of CS1 and CS4. Relatively higher PGA is attributed to lower  
 461 soil thickness below this monitoring point in the CS3 and CS2 models that could be the main



462 reason for acceleration amplification as also stated by Murphy et al. (1971); Beresnev and  
463 Wen (1996).

464 At the middle part of the debris i.e., DB\_Md, relatively higher PGA is attained by the CS2  
465 model (~14.4 m/sec<sup>2</sup>). Notably, despite the relatively higher soil thickness, this monitoring  
466 point obtained a relatively higher PGA. It possibly occurred due to irregular topography of the  
467 CS2 model that generally results in interference of direct and scattered waves and hence  
468 amplification of ground motions (Asimaki and Mohammadi 2018).

469 At the upper part of the debris i.e., DB\_Up, relatively higher PGA is attained by the CS1  
470 model (18.5 m/sec<sup>2</sup>) followed by the CS4 model (15.8 m/sec<sup>2</sup>). The effect of soil thickness  
471 below this monitoring point, as explained for the lower part of debris, could be the main  
472 reason for such amplification at this monitoring point in these models. Monitoring point at  
473 rock mass surface above the landslide crown (CR) too has almost similar PGAs in all the  
474 models except the CS3 model. Relatively higher PGA (10.19 m/sec<sup>2</sup>) at the CR monitoring  
475 point of CS3 model might be due to its position on steeper surface, whereas CR points at  
476 other models are at relatively flat surface.

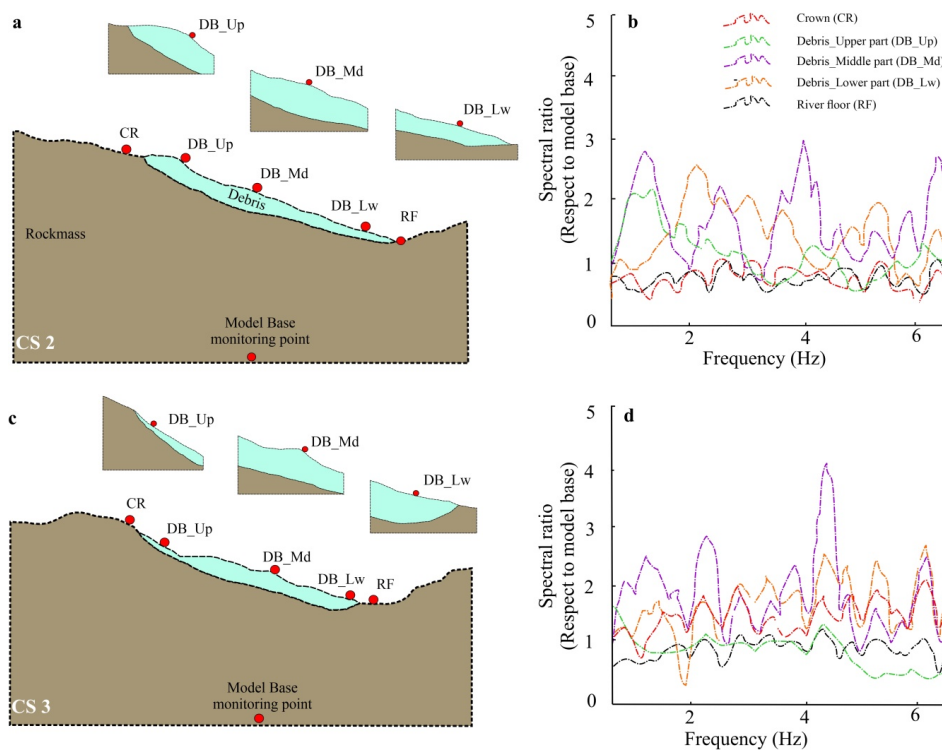
#### 477 4.1.4 Spectral Ratio

478 The ground motion amplifications were also explored using the spectral ratios at two central  
479 slope sections; CS-2 and CS-3 (Fig. 13). In both models, the (River Floor) RF point showed  
480 no significant amplification at any particular frequency, possibly due to the flat surface  
481 positioning. In CS2 model, Debris Lower part (DB\_Lw) point shows notable amplification at  
482 2.0-2.5 Hz with minor amplification at 4.5-5.0 Hz, whereas in the CS 3 model, DB\_Lw point  
483 shows attenuation (or de-amplification) near ~2 Hz and slight amplification at 4.5-6.0 Hz. The  
484 contrast of amplification and de-amplification at ~2 Hz is attributed to the geometrical  
485 variation in topography because the DB\_Lw point in the CS2 is situated at a relatively  
486 elevated surface, whereas in the CS3, at a relatively shallow surface. Minor geometrical  
487 variations at the slope toe have been observed to result in de-amplification at low frequencies  
488 in other studies also (Bouckovalas and Papadimitriou, 2005).

489 Notably, along with the DB\_Lw point, Debris Middle part (DB\_Md) and Debris Upper part  
490 (DB\_Up) points in both the models also have minor/major amplification at 4.5-6.0 Hz. This  
491 coexistence of amplification at a certain frequency range by different monitoring points at  
492 debris surface may be attributed to impedance contrast between debris and underlying rock



493 mass. Further, the DB\_Md point in both the models showed amplification at  $\sim 1.0$  Hz and 2.0-  
494 2.5 Hz. The amplification at lower frequency i.e.,  $\sim 1.0$  Hz may be attributed to the thick (40-  
495 60m) layer of debris that possibly decreases the resonance frequency and results in  
496 amplification of ground motion as also reported by Beresnev and Wen (1996). The  
497 amplification at 2.0-2.5 Hz may be referred to the elevated topography at these points in both  
498 the models.



499

500 **Figure 13:** Spectral ratio pattern. (a) CS-2 model with the position of monitoring points and  
501 zoomed regions of debris monitoring points. (b) Spectral ratio pattern in the CS-2, (c) CS-3  
502 model with the position of monitoring points and zoomed regions of debris monitoring points,  
503 (d) Spectral ratio pattern in the CS-3.

504

505 The DB\_Up point in both the models has different responses. In the CS2 model, it showed  
506 amplification at 1.0-1.5 Hz, whereas in the CS3 model, spectral ratio is relatively stagnant  
507 except minor amplification at 4.0 & 6.0 Hz. This contrast may be understood by the fact that  
508 in the CS2, this monitoring point is situated at a thicker and elevated surface, whereas in the



509 CS3, it is situated at relatively shallow topography and on top of relatively thin landslide  
510 thickness.

511 Finally, the Crown (CR) point also has a different spectral ratio in both the models. It shows  
512 higher amplification in the CS3 model than the CS2 model that may be referred to the  
513 positioning of these points. The CR in the CS2 is situated at a relatively flat surface unlike in  
514 the CS3 model where it is situated at a steep surface. Thus, the monitoring points showed  
515 amplification at multiple frequency range that is attributed to complex topography of  
516 landslide, soil thickness variation, and impedance contrast.

#### 517 4.2 Landslide runout pattern

518 In view of uncertainties to ascertain the exact depth of loose material that will be  
519 eroded/entrained during the debris flow, runout pattern was evaluated at four different depths;  
520 5m, 10m, 15m, and 20m of the loose overburden (Fig. 14a, b). Runout characteristics (flow  
521 height/flow velocity) of the debris flow that will strike the river floor during such an event are  
522 also inferred along the river channel (Fig. 14c).

523 At 5 m soil thickness, the landslide resulted in a maximum flow height of ~8 m and maximum  
524 flow velocity of ~4.5 m/sec (Fig. 14 d, e). Along the river channel, flow attained a maximum  
525 height of ~9 m near the right flank and maximum velocity of ~3 m/sec near the left flank of  
526 the landslide (Fig. 14f). At 10 m soil thickness, the landslide resulted in a maximum flow  
527 height of ~20 m and maximum flow velocity of ~10 m/sec (Fig. 14 g, h). Along the river  
528 channel, flow attained a maximum height of ~16 m and maximum velocity of ~2.9 m/sec near  
529 the right flank (Fig. 14i). At 15 m soil thickness, the landslide resulted in a maximum flow  
530 height of ~30 m and maximum flow velocity of ~16 m/sec (Fig. 14 j, k). Along the river  
531 channel, flow attained a maximum height of ~22 m and maximum velocity of ~2.2 m/sec.  
532 near the right flank (Fig. 14l). At 20 m soil thickness, the landslide resulted in a maximum  
533 flow height of ~42 m and maximum flow velocity of ~21 m/sec (Fig. 14 m, n). Along the  
534 river channel, flow attained a maximum height of ~26 m and maximum velocity of ~2.1  
535 m/sec near the right flank (Fig. 14o).

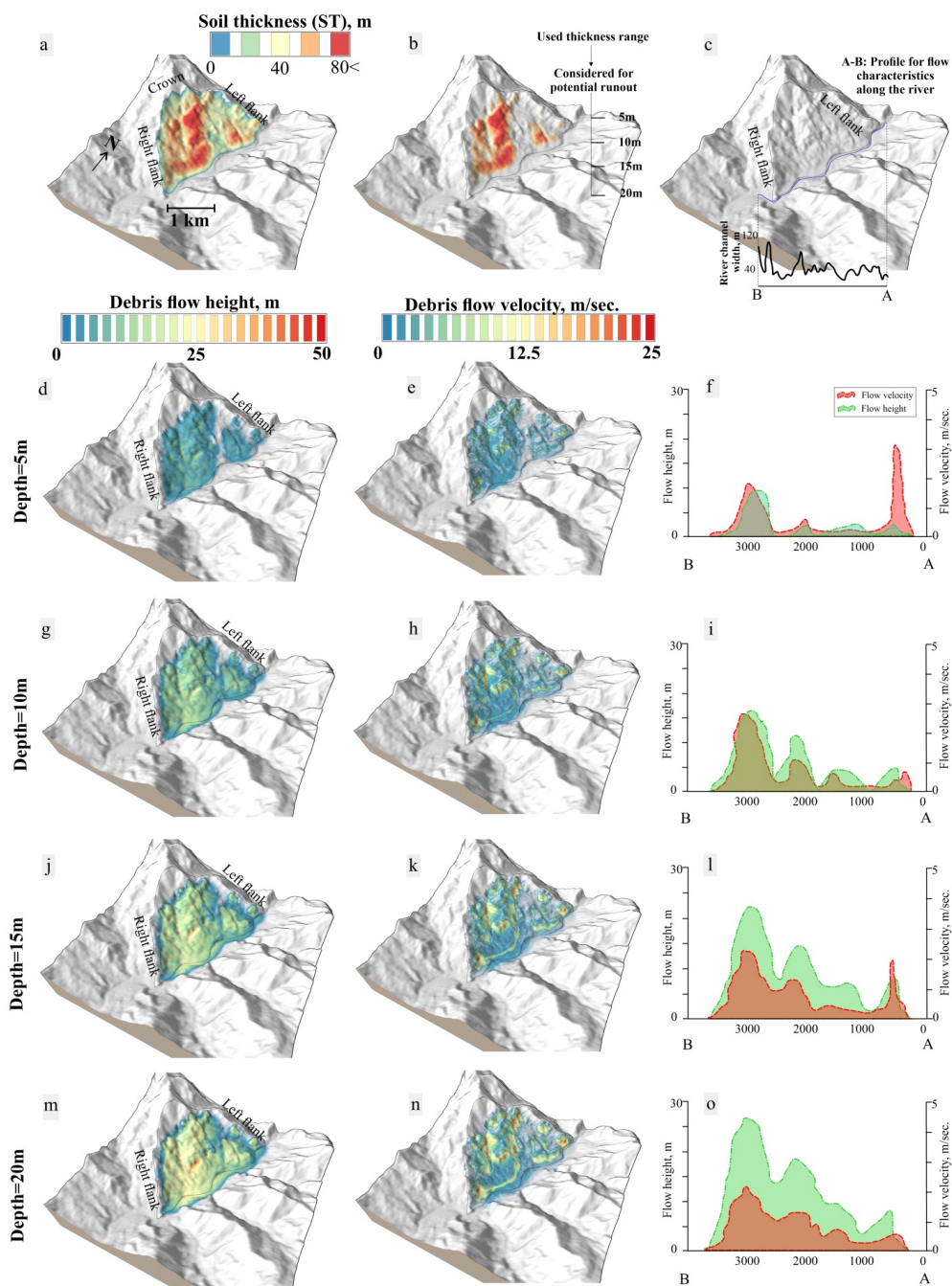
536

537

538

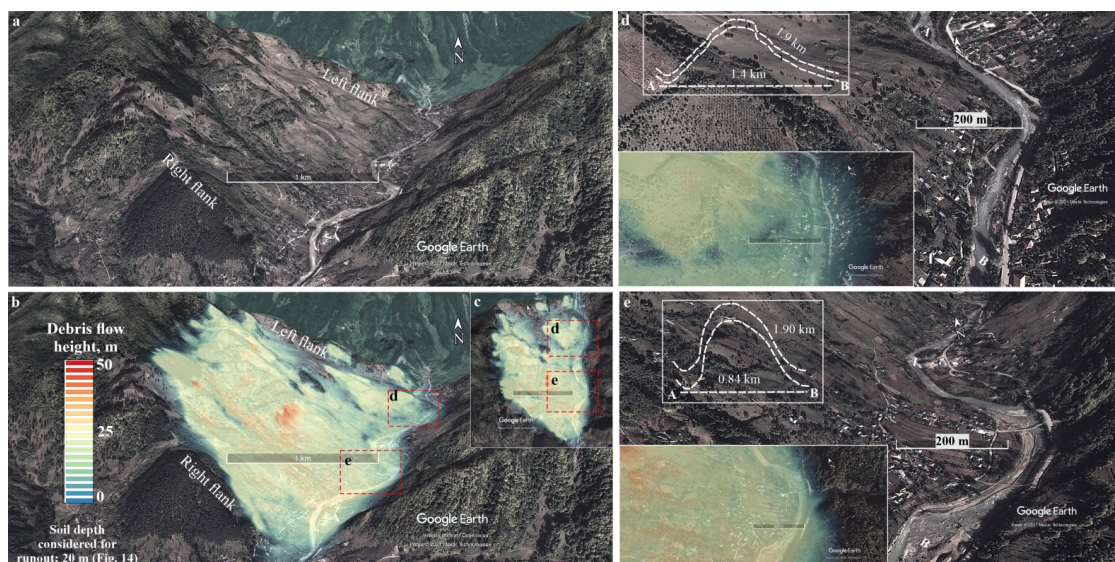


539 **Figure 14:** Debris flow run-out pattern. (a) Soil (or debris) thickness pattern in the landslide,  
 540 (b) Different depths (5, 10, 15, and 20 m) used for the analysis in the 60-80 m thickness  
 541 region, (c) River profile section A-B used to represent the resultant debris flow run-out along  
 542 the river, (d-f) results at 5 m depth, (g-i) results at 10 m depth, (j-l) results at 15 m depth,  
 543 (m-o) results at 20 m depth.





544 Further, in order to understand the extent of runout along the river channel, runout results at  
545 maximum considered thickness (i.e., SE=20 m) were also laid over the Google Earth imagery  
546 (Fig 15a, b). A top view of the landslide with the runout is shown in inset 'c'. The predicted  
547 runout is noted to extend across the river channel mainly at two locations, one near the left  
548 flank (Fig. 15d) and the other near the right flank (Fig. 15e). At both of these locations, the  
549 river channel attains sinuosity in a range of ~1.30-1.32 (shown through channel length  
550 measurement). River channel might owe this sinuosity to the paleo-landslide and/or fluvial  
551 deposit that is extending the slope toe at these locations. Thus, the runout findings of present  
552 study are noted to follow the same spatial extent as possibly followed by previous landslide  
553 events.



554  
555  
556 Fig. 15: Debris flow run-out pattern at 20 m depth. (a) Upstream view of landslide from the  
557 right flank, (b) Run-out pattern at 20 m depth, (c) Top view of landslide highlighting  
558 two regions where runout reached across the river (d) Runout pattern near left flank  
559 extending across the river channel, (e) Runout pattern near right flank extending across  
560 the river channel.

561  
562  
563  
564  
565  
566  
567  
568



## 569 5 SUMMARY

570 The present state of slope reveals an instability condition through the Factor of Safety (FS) in  
571 a range of 1.09-1.32 and potential displacement near the landslide crown (Fig. 9, 10). Such a  
572 displacement near the landslide crown has been related to the development of shear failure in  
573 slopes (Matsui and San, 1992; Kumar et al. 2018; 2021). The possibility of shear failure  
574 becomes more viable in case of degradation of shear strength of slope material and/or rupture  
575 planes. Notably, both the main landslide triggering factors; rainfall and earthquake have been  
576 found to degrade the shear strength of slope material through the percolation and shaking  
577 induced particle movements, respectively (Cai and Ugai, 2004; Chang and Taboada 2009).

578 The GW, implying the rainfall induced percolation effect, further decreases the Factor of  
579 Safety and increases the material displacement (Fig. 9, 10). This effect of the GW is attributed  
580 to the hydraulic pressure in the joint against the overlying loose material that decreases the  
581 normal stress and hence the shear strength of overlying loose material (Mohr, 1914;  
582 Witherspoon et al. 1980).

583 Similar to the GW effect in static condition, the combined response of the dynamic force and  
584 the GW resulted in an increase of the displacement (Fig. 9). Increased displacement during  
585 the seismic force can be understood from the following equation (Cundall 1980);  
586

$$587 \quad \mathbf{u} = \left( \frac{\int(\sigma.n.ds+F)}{m} \right) + \mathbf{g} \quad \text{Eq. 4}$$

588 Here,  $\mathbf{u}$ = displacement,  $\sigma$ = zone stress tensor,  $s$ = surface enclosing the mass ( $m$ ),  $n$ = unit  
589 normal to  $s$ ,  $g$ = gravitational acceleration,  $F$ = resultant force ( $F^z+ F^c+ F^e$ ).  $F^z$  = internal stress  
590 in zone,  $F^c$  = contact forces between blocks (joint),  $F^e$  = external force. Here, seismic force is  
591 represented by the  $F^e$ .

592 The enhanced material displacement during the combined effect of the dynamic force and the  
593 GW can be attributed to the fact that seismic shaking increases the hydraulic pressure in the  
594 joints that causes enhanced material displacement in the overlying loose material (Wang et al.  
595 2010).

596 Apart from the Factor of Safety (FS) and material displacement, ground motion amplification  
597 also revealed slope instability (or potential deformation). The maximum value of Peak



598 Ground Acceleration (PGA) is attained by the upper part of the debris surface (near the  
599 landslide crown) (Fig. 12) that is referred to the impedance contrast between underlying rock  
600 mass and overlying soil and/or partial loss of the shear strength during seismicity (Novak and  
601 Yan, 1990; Safak, 2001). Further, the spectral ratio also showed signal amplification, at  
602 multiple frequency range, at the debris surface (Fig. 13). Such amplification at multiple  
603 frequency ranges is attributed to complex topography of landslide, soil thickness variation,  
604 and impedance contrast (sec. 4.1.4). Such high amplification at the slope surface has been  
605 considered as a main cause of slope failure in many studies (Lenti and Martino, 2012; Gaudio  
606 et al. 2014).

607 As also stated in sec. 3.3, hillslopes affected by the seismic shaking have also been prone to  
608 rainfall induced failures, particularly in the form of debris flows. Further, the earthquake  
609 induced shear strength degradation of slope material may also result in the enhanced  
610 entrainment during a debris flow event (Liu et al. 2020). These debris flows might be initiated  
611 either by increased pore pressure (or GW induced hydraulic pressure) or runoff involving  
612 entrainment (Godt and Coe 2007). Though the GW effect is obtained on the slope instability  
613 (Fig. 9, 10), potential response of the slope under excessive rainfall is explored through debris  
614 flow runout analysis (Fig. 14, 15).

615 The debris flow runout predictions revealed a non-linear increase in the debris flow height  
616 (9.0-26.0 m) and velocity (2.1-3.0 m/sec.) along the river channel on using the increasing  
617 thickness (5, 10, 15, and 20 m) of erodible material (Fig. 14). This non-linearity is attributed to  
618 the downstream variation of the river channel width (Fig. 14c) and influx of debris flow  
619 material from the slope. Though the present study noted the influence of channel morphology  
620 on the debris flow characteristics, other studies have observed the changes in channel  
621 morphology caused by the debris flows (Remaître et al., 2005; Simoni et al. 2020).

622 Thus, there seems to be a positive feedback process between channel morphology and debris  
623 flow. This feedback notion is further strengthened by the finding of debris flow extent across  
624 the river channel (Fig. 15d, e). At both of these locations, slope toe extends towards the E-SE  
625 direction resulting in higher channel sinuosity. These extended slope toes probably represent  
626 paleo-landslide and/or fluvial deposits. Signs of flow relics at the slope surface & failure at  
627 slope toe at these locations (Fig. 2d,e) further support the possibility of paleo-landslide  
628 deposit. Thus, the predicted extent of potential debris flow is found to follow the trails created  
629 by previous landslide flow and/or slide events. Aforementioned findings, temporally



630 increasing rainfall, soil moisture, and surface runoff (sec. 2.2), and frequent debris flows/flash  
631 floods in this region (Micu et al. 2013; Grecu et al. 2017; Micu et al. 2019) pose increasing  
632 risk caused by debris flow in the study area.

633 Finally, there are still some uncertainties in such predictive approaches that are as follows; (1)  
634 inclusion of subsurface discontinuity network, spatially varying groundwater surface, and  
635 material heterogeneity in the 3D model, (2) inclusion of variable depth and phases in the  
636 runout modeling. Despite these possible uncertainties, which will be overcome in future  
637 prospects, such studies are required to minimize the risk and avert the possible disasters.

## 638 **6 CONCLUSIONS**

639 By utilizing field based data and numerical simulations of a massive (~9.1 Mm<sup>2</sup>) ‘Varlaam’  
640 landslide in the SE Carpathians (Romania), present study explored the potential response of  
641 this landslide in seismic and rainfall regime.

642 The slope revealed the Factor of Safety (FS) in a range of 1.17-1.32 with a displacement of  
643 0.4-4 m (under gravity load) that increases up to 8-60 m under seismic force. The  
644 Groundwater (GW) further decreased the slope stability. The GW effect is attributed to the  
645 hydraulic pressure in the joint against the overlying loose material that decreased the normal  
646 stress and hence the shear strength of overlying loose material. Ground motion amplification,  
647 during seismic shaking, further revealed the potential instability of slope with a Peak Ground  
648 Acceleration (PGA) on the slope surface in a range of 0.65g - 1.88g. Such amplification  
649 pertains to complex topography of landslide, soil thickness variation, and impedance contrast.

650 Further, though the GW effect is obtained on the slope instability, potential response of the  
651 slope under excessive rainfall is also evaluated through debris flow runout analysis. The  
652 predicted debris flow revealed a non-linear increase in the debris flow height (9.0-26.0 m) and  
653 velocity (2.1-3.0 m/sec) along the river channel. This variation along the river channel is  
654 attributed to the river channel morphology and influx of debris flow material from the slope.  
655 Owing to the predictive nature of present study, the concept may be applied in other terrains  
656 subjected to frequent landslides mostly triggered by extreme rainfall & earthquakes.

657 **Author contribution:** VK and HBH conceived the idea. All authors participated in the field  
658 data collection & data interpretation. VK, LC, and ASM performed the numerical simulations.



659 MM led the geomorphic interpretation. All authors contributed to the writing of the final  
660 draft.

661 **Competing interests:** The authors declare that they have no conflict of interest.

662 **Financial support:** Authors are thankful for the financial grant by the F.R.S.–FNRS Belgium  
663 in the frame of the Belgian-Swiss collaboration project ‘4D seismic response and slope  
664 failure’.

#### 665 **ACKNOWLEDGEMENT**

666 Authors acknowledge Philippe Cerfontaine, Martin Depret, Nirmal Dhabaria and George  
667 Catalin Simion for data acquisition (DGPS and seismological measurements).

#### 668 **REFERENCES**

- 669 Apostol, L.:The Mediterranean cyclones–the role in ensuring water resources and their potential of Apostol, L.,  
670 2008. The Mediterranean cyclones–the role in ensuring water resources and their potential of climatic  
671 risk, in the east of Romania. Present environment and sustainable development, 2, pp.143-163, 2008.
- 672 Asimaki, D. and Mohammadi, K.: On the complexity of seismic waves trapped in irregular topographies. Soil  
673 Dynamics and Earthquake Engineering, 114, 424-437, 2018.
- 674 Barton, N. and Choubey, V.:The shear strength of rock joints in theory and practice. Rock mechanics, 10(1), 1-  
675 54, 1977.
- 676 Barton, N. R.:A model study of rock-joint deformation, Int. J. Rock Mech. Min., 9, 579–602, 1972.
- 677 Bednarczyk, Z.: Identification of flysch landslide triggers using conventional and ‘nearly real-time’ monitoring  
678 methods–An example from the Carpathian Mountains, Poland. Engineering Geology, 244, 41-56, 2018.
- 679 Beguería, S., Van Asch, T.W., Malet, J.P. and Gröndahl, S.:A GIS-based numerical model for simulating the  
680 kinematics of mud and debris flows over complex terrain. Natural Hazards and Earth System Sciences,  
681 9(6), pp.1897-1909, 2009.
- 682 Beresnev, I.A. and Wen, K.L.:Nonlinear soil response—A reality?. Bulletin of the Seismological Society of  
683 America, 86(6), pp.1964-1978, 1996.
- 684 Bhasin, R. and Kaynia, A.M.:Static and dynamic simulation of a 700-m high rock slope in western Norway.  
685 Engineering Geology, 71(3-4), pp.213-226, 2004.
- 686 Biggs, J.M. and Biggs, J.: Introduction to structural dynamics. McGraw-Hill College. 1964.
- 687 Bokelmann, G. and Rodler, F.A.:Nature of the Vrancea seismic zone (Eastern Carpathians)–New constraints  
688 from dispersion of first-arriving P-waves. Earth and Planetary Science Letters, 390, 59-68, 2014.
- 689 Bontemps, N., Lacroix, P., Larose, E., Jara, J. and Taïpe, E.:Rain and small earthquakes maintain a slow-moving  
690 landslide in a persistent critical state. Nature communications, 11(1), pp.1-10, 2020.
- 691 Bouckovalas, G.D. and Papadimitriou, A.G.:Numerical evaluation of slope topography effects on seismic ground  
692 motion. Soil Dynamics and Earthquake Engineering, 25(7-10), 547-558, 2005.
- 693 Bourdeau, C. and Havenith, H.B.: Site effects modelling applied to the slope affected by the Suusamyr  
694 earthquake (Kyrgyzstan, 1992). Engineering Geology, 97(3-4), 126-145, 2008.
- 695 Cai, F. and Ugai, K.: Numerical analysis of rainfall effects on slope stability. International Journal of  
696 Geomechanics, 4(2), pp.69-78, 2004.



- 697 Cauchie, L., Mreyen, A.S., Micu, M., Cerfontaine, P. and Havenith, H.B.: Landslide characterization by seismic  
698 ambient noise analysis: application to Carpathian Mountains. In AGU Fall Meeting,  
699 DOI:10.13140/RG.2.2.18971.69924, 2019.
- 700 Chang, K.J. and Taboada, A.: Discrete element simulation of the Jiufengershan rock-and-soil avalanche  
701 triggered by the 1999 Chi-Chi earthquake, Taiwan. *Journal of Geophysical Research: Earth Surface*,  
702 114(F3), 2009.
- 703 Christen, M., Kowalski, J. and Bartelt, P.:RAMMS: Numerical simulation of dense snow avalanches in three-  
704 dimensional terrain. *Cold Regions Science and Technology*, 63(1-2), 1-14, 2010.
- 705 Constantin, S., Bojar, A.V., Lauritzen, S.E. and Lundberg, J.:Holocene and Late Pleistocene climate in the sub-  
706 Mediterranean continental environment: A speleothem record from Poleva Cave (Southern Carpathians,  
707 Romania). *Palaeogeography, Palaeoclimatology, Palaeoecology*, 243(3-4), 322-338, 2007.
- 708 Coulomb, C. A.: An attempt to apply the rules of maxima and minima to several problems of stability related to  
709 architecture”. *Mémoires de l’Académie Royale des Sciences* 7: 343-382, 1776.
- 710 Croitoru, A.E., Piticar, A. and Burada, D.C. :Changes in precipitation extremes in Romania. *Quaternary*  
711 *International*, 415, pp.325-335, 2016.
- 712 Cundall, P.A.: UDEC-A Generalised Distinct Element Program for Modelling Jointed Rock. Cundall (Peter)  
713 Associates Virginia Water (England), 1980.
- 714 Ding, M., Huang, T., Zheng, H. and Yang, G.:Respective influence of vertical mountain differentiation on debris  
715 flow occurrence in the Upper Min River, China. *Scientific Reports*, 10(1), 1-13, 2020.
- 716 Durand, V., Mangeney, A., Haas, F., Jia, X., Bonilla, F., Peltier, A., Hibert, C., Ferrazzini, V., Kowalski, P.,  
717 Laurent, F. and Brunet, C.: On the link between external forcings and slope instabilities in the Piton de la  
718 Fournaise Summit Crater, Reunion Island. *Journal of Geophysical Research: Earth Surface*, 123(10),  
719 2422-2442, 2018.
- 720 Fell, R. and Hartford, D.: Landslide risk management. *Landslide risk assessment*, 51, 109, 1997.
- 721 Fenton, G.A. and Griffiths, D.V.: Risk assessment in geotechnical engineering (Vol. 461). New York: John  
722 Wiley & Sons, 2008.
- 723 Froude, M.J. and Petley, D.N.: Global fatal landslide occurrence from 2004 to 2016. *Natural Hazards and Earth*  
724 *System Sciences*, 18(8), 2161-2181, 2018.
- 725 Gaudio, V.D., Zhao, B., Luo, Y., Wang, Y. and Wasowski, J.: Seismic response of steep slopes inferred from  
726 ambient noise and accelerometer recordings: the case of Dadu River valley, China. *Engineering Geology*,  
727 259, 105197, 2019.
- 728 Gholamy, A. and Kreinovich, V.: Why Ricker wavelets are successful in processing seismic data: Towards a  
729 theoretical explanation. In 2014 IEEE Symposium on Computational Intelligence for Engineering  
730 Solutions (CIES) (pp. 11-16). IEEE, 2014.
- 731 Godt, J.W. and Coe, J.A.: Alpine debris flows triggered by a 28 July 1999 thunderstorm in the central Front  
732 Range, Colorado. *Geomorphology*, 84(1-2), 80-97, 2007.
- 733 Grecu, F., Zaharia, L., Ioana-Toroimac, G. and Armaş, I.: Floods and flash-floods related to river channel  
734 dynamics. In *Landform dynamics and evolution in Romania* (pp. 821-844). Springer, Cham., 2017.
- 735 Griffiths, D.V. and Lane, P.A.: Slope stability analysis by finite elements. *Geotechnique*, 49(3), 387-403, 1999.
- 736 Haque, U., Da Silva, P.F., Devoli, G., Pilz, J., Zhao, B., Khaloua, A., Wilopo, W., Andersen, P., Lu, P., Lee, J.  
737 and Yamamoto, T.: The human cost of global warming: Deadly landslides and their triggers (1995–2014).  
738 *Science of the Total Environment*, 682, 673-684, 2019.
- 739 Hara, A., Ohta, T., Niwa, M., Tanaka, S. and Banno, T.: Shear modulus and shear strength of cohesive soils.  
740 *Soils and Foundations*, 14(3),1-12, 1974.



- 741 Havenith, H.B., Strom, A., Calvetti, F. and Jongmans, D.: Seismic triggering of landslides. Part B: Simulation of  
742 dynamic failure processes. *Natural Hazards and Earth System Sciences*, 3(6), 663-682, 2003.
- 743 Havenith, H.B., Torgoev, A., Braun, A., Schlögel, R. and Micu, M.: A new classification of earthquake-induced  
744 landslide event sizes based on seismotectonic, topographic, climatic and geologic factors.  
745 *Geoenvironmental Disasters*, 3(1), 1-24, 2016.
- 746 Helmstetter, A. and Garambois, S.: Seismic monitoring of Séchilienne rockslide (French Alps): Analysis of  
747 seismic signals and their correlation with rainfalls. *Journal of Geophysical Research: Earth Surface*,  
748 115(F3), 2010.
- 749 Hoek, E. and Brown, E.T.: Practical estimates of rock mass strength. *International journal of rock mechanics and*  
750 *mining sciences*, 34(8), 1165-1186, 1997.
- 751 Hoek, E. and Diederichs, M.S.: Empirical estimation of rock mass modulus. *International journal of rock*  
752 *mechanics and mining sciences*, 43(2), 203-215, 2006.
- 753 Hoek, E., Carranza-Torres, C. and Corkum, B.: Hoek-Brown failure criterion-2002 edition. *Proceedings of*  
754 *NARMS-Tac*, 1(1), 267-273, 2002.
- 755 Huffman, G.J., Stocker, E.F., Bolvin, D.T., Nelkin, E.J. and Jackson T.: GPM IMERG Final Precipitation L3 1  
756 day 0.1 degree x 0.1 degree V06, Edited by Andrey Savtchenko, Greenbelt, MD, Goddard Earth Sciences  
757 Data and Information Services Center (GES DISC), Accessed: Sep. 5, 2020,  
758 10.5067/GPM/IMERGDF/DAY/06, 2019.
- 759 Hungr, O.: A review of landslide hazard and risk assessment methodology. *Landslides and engineered slopes.*  
760 *Experience, theory and practice*, edited by: Aversa, S., Cascini, L., Picarelli, L., and Scavia, C., CRC  
761 Press, Boca Raton, FL, 3-27, 2018.
- 762 Hungr, O., Morgan, GC and Kellerhals, R.: Quantitative analysis of debris torrent hazards for design of remedial  
763 measures. *Canadian Geotechnical Journal*, 21 (4), 663-677, 1984.
- 764 Hürlimann, M., Rickenmann, D., Medina, V. and Bateman, A.: Evaluation of approaches to calculate debris-  
765 flow parameters for hazard assessment. *Engineering Geology*, 102(3-4), 152-163, 2008.
- 766 Hutter, K., Svendsen, B. and Rickenmann, D.: Debris flow modeling: A review. *Continuum mechanics and*  
767 *thermodynamics*, 8(1), 1-35, 1994.
- 768 Ibs-von Seht, M. and Wohlenberg, J.: Microtremor measurements used to map thickness of soft sediments.  
769 *Bulletin of the Seismological Society of America*, 89(1), 250-259, 1999.
- 770 Ilinca, V.: Characteristics of debris flows from the lower part of the Lotru River basin (South Carpathians,  
771 Romania). *Landslides*, 11(3), 505-512, 2014.
- 772 Jakob, M., Hungr, O. and Jakob, D.M.: *Debris-flow hazards and related phenomena (Vol. 739)*. Berlin:  
773 Springer., 2005.
- 774 Jamir, I., Gupta, V., Kumar, V. and Thong, G.T.: Evaluation of potential surface instability using finite element  
775 method in Kharsali Village, Yamuna Valley, Northwest Himalaya. *Journal of Mountain Science*,  
776 14(8),1666-1676, 2017.
- 777 Jibson, R.: Summary of research on the effects of topographic amplification of earthquake shaking on slope  
778 stability. *US Geological Survey*, 87-269, 1987.
- 779 Jing, L.: A review of techniques, advances and outstanding issues in numerical modelling for rock mechanics  
780 and rock engineering. *International Journal of Rock Mechanics and Mining Sciences*, 40(3), 283-353,  
781 2003.
- 782 Kahraman, S.: Evaluation of simple methods for assessing the uniaxial compressive strength of rock.  
783 *International Journal of Rock Mechanics and Mining Sciences*, 38(7), 981-994, 2001.



- 784 Klimeš, J., Rosario, A.M., Vargas, R., Raška, P., Vicuña, L. and Jurt, C.: Community participation in landslide  
785 risk reduction: a case history from Central Andes, Peru. *Landslides*, 16(9), 1763-1777, 2019.
- 786 Kuhlemeyer, R.L. and Lysmer, J.: Finite element method accuracy for wave propagation problems. *Journal of*  
787 *Soil Mechanics & Foundations Div*, 99(Tech Rpt), 1973.
- 788 Kumar, V., Gupta, V. and Jamir, I.: Hazard evaluation of progressive Pawari landslide zone, Satluj valley,  
789 Himachal Pradesh, India. *Natural Hazards*, 93(2), 1029-1047, 2018.
- 790 Kumar, V., Jamir, I., Gupta, V. and Bhasin, R.K.: Inferring potential landslide damming using slope stability,  
791 geomorphic constraints and run-out analysis; case study from the NW Himalaya. *Earth Surface*  
792 *Dynamics*, 9(2), 351-377, 2021.
- 793 Lenti, L., Martino, S.: The interaction of seismic waves with step-like slopes and its influence on landslide  
794 movements. *Eng. Geol.* 126, 19–36, 2012.
- 795 Li, B., Beaudoin, H. and Rodell, M. : GLDAS Catchment Land Surface Model L4 daily 0.25 x 0.25 degree  
796 GRACE-DA1 V2.2, Greenbelt, Maryland, USA, Goddard Earth Sciences Data and Information Services  
797 Center (GES DISC), Accessed: Sep. 5, 2020, 10.5067/TXBMLX370XX8, 2020.
- 798 Liang, W.L.: Dynamics of pore water pressure at the soil–bedrock interface recorded during a rainfall-induced  
799 shallow landslide in a steep natural forested headwater catchment, Taiwan. *Journal of Hydrology*, 587,  
800 125003, 2020.
- 801 Lin, C.W., Liu, S.H., Lee, S.Y. and Liu, C.C.: Impacts of the Chi-Chi earthquake on subsequent rainfall-induced  
802 landslides in central Taiwan. *Engineering Geology*, 86(2-3), 87-101, 2006.
- 803 Liu, Z., Su, L., Zhang, C., Iqbal, J., Hu, B. and Dong, Z.: Investigation of the dynamic process of the Xinmo  
804 landslide using the discrete element method. *Computers and Geotechnics*, 123, p.103561, 2020.
- 805 Luo, Y., Fan, X., Huang, R., Wang, Y., Yunus, A.P. and Havenith, H.B.: Topographic and near-surface  
806 stratigraphic amplification of the seismic response of a mountain slope revealed by field monitoring and  
807 numerical simulations. *Engineering Geology*, 271, p.105607, 2020.
- 808 Magyari, E.K., Demény, A., Buczkó, K., Kern, Z., Vennemann, T., Fórizs, I., Vincze, I., Braun, M., Kovács, J.I.,  
809 Udvardi, B. and Veres, D.: A 13,600-year diatom oxygen isotope record from the South Carpathians  
810 (Romania): Reflection of winter conditions and possible links with North Atlantic circulation changes.  
811 *Quaternary International*, 293, 136-149, 2013.
- 812 Margottini, C., Canuti, P. and Sassa, K.: *Landslide science and practice (Vol. 1)*. Berlin: Springer, 2013.
- 813 Mațenco, L.: Tectonics and exhumation of Romanian Carpathians: inferences from kinematic and  
814 thermochronology studies. In *Landform dynamics and evolution in Romania* (pp. 15-56). Springer,  
815 Cham., 2017.
- 816 Matsui, T. and San, K.C.: Finite element slope stability analysis by shear strength reduction technique. *Soils and*  
817 *foundations*, 32(1), 59-70, 1992.
- 818 McDowell, P.W.: The determination of the dynamic elastic moduli of rock masses by geophysical methods.  
819 *Geological Society, London, Engineering Geology Special Publications*, 6(1), 267-274, 1990.
- 820 McNally, A., Arsenault, K., Kumar, S., Shukla, S., Peterson, P., Wang, S., Funk, C., Peters-Lidard, C.D. and  
821 Verdin, J.P.: A land data assimilation system for sub-Saharan Africa food and water security applications.  
822 *Scientific data*, 4(1), 1-19, 2017.
- 823 Micu, M.: Landslide hazard assessment in Vrancea seismic region (Curvature Carpathians of Romania):  
824 achievements and perspectives. In *1<sup>st</sup> EAGE Workshop on Assessment of Landslide and Debris Flows*  
825 *Hazards in the Carpathians*, 1-5, 2019.
- 826 Micu, M., Jurchescu, M., Șandric, I., Mărgărint, C., Zenaida, C., Dana, M., Ciurean, R., Ilinca, V., Vasile, M.:  
827 Natural Risks - Mass Movements, in M. Radoane, A. Vespremeanu-Stroe (Eds.) *Landform dynamics and*  
828 *evolution in Romania*, Springer, 765-820, 2016.



- 829 Micu, M., Bălăceanu, D., Micu, D., Zarea, R. and Raluca, R.: Landslides in the Romanian Curvature Carpathians  
830 in 2010. In *Geomorphological impacts of extreme weather*, Springer, Dordrecht, 251-264, 2013.
- 831 Mohr, O.: *Abhandlungen aus dem Gebiete der Technischen Mechanik* (2nd ed). Ernst, Berlin, 1914.
- 832 Mreyen, A.S., Cauchie, L., Micu, M., Onaca, A. and Havenith, H.B.: Multiple geophysical investigations to  
833 characterize massive slope failure deposits: application to the Balta rockslide, Carpathians. *Geophysical*  
834 *Journal International*, 225(2), 1032-1047, 2021.
- 835 Murgeanu, G., Dumitrescu, I., Sandulescu, M., Bandrabur, T. and Sandulesu, J.: *Harta geologică a RS România.*  
836 *L-35-XXI, scara 1: 200.000, Foaia Covasna*, 1965.
- 837 Murphy, J.R., Davis, A.H. and Weaver, N.L.: Amplification of seismic body waves by low-velocity surface  
838 layers. *Bulletin of the Seismological Society of America*, 61(1), 109-145, 1971.
- 839 Nakamura, Y.: Basic structure of QTS (HVSr) and examples of applications. In *Increasing seismic Safety by*  
840 *combining engineering technologies and seismological data*, Springer, Dordrecht., 33-51, 2009.
- 841 Novak, M. and Han, Y.C.: Impedances of soil layer with boundary zone. *Journal of geotechnical engineering*,  
842 116(6), 1008-1014, 1990.
- 843 Obrecht, I., Zeeden, C., Hambach, U., Veres, D., Marković, S.B., Böskén, J., Svirčev, Z., Bačević, N., Gavrilov,  
844 M.B. and Lehmkühl, F.: Tracing the influence of Mediterranean climate on Southeastern Europe during  
845 the past 350,000 years. *Scientific Reports*, 6(1), 1-10, 2016.
- 846 O'Brien, J.S., Julien, P.Y. and Fullerton, W.T.: Two-dimensional water flood and mudflow simulation. *Journal*  
847 *of hydraulic engineering*, 119(2), 244-261, 1993.
- 848 Peranić, J., Moscariello, M., Cuomo, S. and Arbanas, Ž.: Hydro-mechanical properties of unsaturated residual  
849 soil from a flysch rock mass. *Engineering Geology*, 269, 105546, 2020.
- 850 Petrescu, L., Stuart, G., Tataru, D. and Grecu, B.: Crustal structure of the Carpathian Orogen in Romania from  
851 receiver functions and ambient noise tomography: how craton collision, subduction and detachment affect  
852 the crust. *Geophysical Journal International*, 218(1), 163-178, 2019.
- 853 Pollock, W. and Wartman, J.: Human vulnerability to landslides. *Geohealth*, 4(10), p.e2020GH000287, 2020.
- 854 Pospíšil, L., Hefty, J. and Hipmanová, L.: Risk and geodynamically active areas of the Carpathian lithosphere on  
855 the base of geodetical and geophysical data. *Acta Geodaetica et Geophysica Hungarica*, 47(3), 287-309,  
856 2012.
- 857 Radulian, M., Bonjer, K.P., Popa, M. and Popescu, E.: Seismicity patterns in SE Carpathians at crustal and  
858 subcrustal domains: tectonic and geodynamic implications. In *Proceedings of the International*  
859 *Symposium on Strong Vrancea Earthquakes and Risk Mitigation*, Bucharest, Romania, 4-6, 2007.
- 860 Remaître, A., Malet, J.P. and Maquaire, O. : Morphology and sedimentology of a complex debris flow in a clay-  
861 shale basin. *Earth surface processes and landforms*, 30(3), 339-348, 2005.
- 862 Rickenmann, D. and Scheidl, C.: Debris-flow runout and deposition on the fan. In *Dating torrential processes on*  
863 *fans and cones*, Springer, Dordrecht, 75-93, 2013.
- 864 Ricker, N.: Further developments in the wavelet theory of seismogram structure. *Bulletin of the Seismological*  
865 *Society of America*, 33(3), 197-228, 1943.
- 866 Şafak, E.: Local site effects and dynamic soil behavior. *Soil Dynamics and Earthquake Engineering*, 21(5), 453-  
867 458, 2001.
- 868 Sassa, K.: ISDR-ICL Sendai Partnerships 2015–2025 for global promotion of understanding and reducing  
869 landslide disaster risk. *Landslides*, 12(4), 631-640, 2015.
- 870 Shieh, C.L., Chen, Y.S., Tsai, Y.J. and Wu, J.H.: Variability in rainfall threshold for debris flow after the Chi-  
871 Chi earthquake in central Taiwan, China. *International Journal of Sediment Research*, 24(2), 177-188,  
872 2009.



- 873 Simoni, A., Bernard, M., Berti, M., Boreggio, M., Lanzoni, S., Stancanelli, L.M. and Gregoretto, C.: Runoff-  
874 generated debris flows: Observation of initiation conditions and erosion–deposition dynamics along the  
875 channel at Cancia (eastern Italian Alps). *Earth Surface Processes and Landforms*, 45(14), 3556-3571,  
876 2020.
- 877 Tang, C., Zhu, J., Qi, X. and Ding, J.: Landslides induced by the Wenchuan earthquake and the subsequent  
878 strong rainfall event: A case study in the Beichuan area of China. *Engineering Geology*, 122(1-2), 22-33,  
879 2011.
- 880 Tischler, M., Matenco, L., Filipescu, S., Gröger, H.R., Wetzel, A. and Fügenschuh, B.: Tectonics and  
881 sedimentation during convergence of the ALCAPA and Tisza–Dacia continental blocks: the Pienide  
882 nappe emplacement and its foredeep (N. Romania). *Geological Society, London, Special Publications*,  
883 298(1), 317-334, 2008.
- 884 Ustaszewski, K., Schmid, S.M., Fügenschuh, B., Tischler, M., Kissling, E. and Spakman, W.: A map-view  
885 restoration of the Alpine-Carpathian-Dinaridic system for the Early Miocene. *Swiss Journal of*  
886 *Geosciences*, 101(1), 273-294, 2008.
- 887 Van Asch, T.W., Buma, J. and Van Beek, L.P.H.: A view on some hydrological triggering systems in landslides.  
888 *Geomorphology*, 30(1-2), 25-32, 1999.
- 889 Van Westen, C.J., Van Asch, T.W. and Soeters, R.: Landslide hazard and risk zonation—why is it still so  
890 difficult? *Bulletin of Engineering geology and the Environment*, 65(2), 167-184, 2006.
- 891 Wang, G., Suemine, A. and Schulz, W.H.: Shear-rate-dependent strength control on the dynamics of rainfall-  
892 triggered landslides, Tokushima Prefecture, Japan. *Earth Surface Processes and Landforms*, 35(4), 407-  
893 416, 2010.
- 894 Witherspoon, P.A., Wang, J.S., Iwai, K. and Gale, J.E.: Validity of cubic law for fluid flow in a deformable rock  
895 fracture. *Water resources research*, 16(6), 1016-1024, 1980.
- 896
- 897
- 898